

An Optical, Near-Infrared, and Kinematic Study of Four Early-Type
Resonance Ring Galaxies

Ronald Buta – University of Alabama
et al.

Deposited 07/09/2019

Citation of published version:

Buta, R., Aflert, A., Cobb, M., Crocker, D., Purcell, G. (1998): An Optical, Near-Infrared, and Kinematic Study of Four Early-Type Resonance Ring Galaxies. *The Astronomical Journal*, 116(3). DOI: [10.1086/300494](https://doi.org/10.1086/300494)

AN OPTICAL, NEAR-INFRARED, AND KINEMATIC STUDY OF FOUR EARLY-TYPE RESONANCE RING GALAXIES

R. BUTA,^{1,2} ADINA J. ALPERT,³ MELINDA LEWIS COBB,⁴ D. A. CROCKER,^{1,2} AND GUY B. PURCELL^{1,2}

Received 1998 March 5; revised 1998 May 26

ABSTRACT

We present optical and near-infrared surface photometry of four early-type galaxies considered to have resonance ring phenomena on the basis of morphology. We also present kinematics and rotation curves for three of the galaxies. The four galaxies are exceptional examples of resonance ring galaxies, and from these observations we derive the characteristic light distributions, the colors of the rings, and the near-infrared disk mass-to-light ratios. We also deproject the galaxies to examine intrinsic ring shapes and bar/ring alignments. From models of the rotation curves, we compute the Lindblad precession frequencies to examine resonance locations in the disks of the galaxies. Under the assumption that the outer rings and pseudorings seen in these galaxies are linked to the outer Lindblad resonance, we find that the inner rings of the sample galaxies lie near the inner 4:1 resonance and that the sharp ends of the bars lie on average at only 0.65 times the predicted radius of corotation.

Key words: galaxies: individual (NGC 1326, IC 4290, ESO 509-98, ESO 566-24) — galaxies: ISM — galaxies: photometry — galaxies: structure

1. INTRODUCTION

Early-type galaxies provide the strongest examples of inner, outer, and nuclear ring phenomena among the population of normal disk galaxies. Multiple rings occur commonly among these galaxies, and the characteristics of the rings are so distinctive that they can be linked morphologically to specific orbital resonances with a bar or oval in the mass distribution (hence the term “resonance ring” galaxies). These galaxies are important subjects for detailed study, because the rings act as probes of internal barred galaxy dynamics, the properties of which have not yet been fully tapped for what they can tell us about galaxies as a whole. As more ringed galaxies are studied in detail, it is becoming clear that there is so much diversity within the class that any theory of the dynamics and evolution of barred galaxies must be considered inadequate until such diversity is explained.

In this paper, we examine the detailed optical and near-infrared photometric characteristics of four exceptional early-type ringed galaxies selected from the Catalog of Southern Ringed Galaxies (Buta 1995, hereafter CSRG). The four galaxies, NGC 1326, IC 4290, ESO 509-98, and ESO 566-24, are exceptional mainly in the strength and symmetry of their features, and are not typical CSRG galaxies. We chose them because they can best highlight the distinctive features of resonance rings and provide insights into the mass distributions that characterize such galaxies. This paper is one of several in preparation concerning CSRG galaxies. In approach this paper is similar to the study of NGC 3081 by Buta & Purcell (1998, hereafter

BP98). We begin by discussing in § 2 the optical morphological properties of the sample galaxies, and then summarize the observations in § 3. Section 4 describes the near-infrared morphologies of the galaxies and presents color index maps. The surface photometry is presented in § 5, and the Fabry-Perot interferometry in § 6. The deprojected structure of the galaxies is discussed in § 7. In § 8, we use the near-IR data to estimate the gravitational potentials in the galaxies, and by linking outer rings to the outer Lindblad resonance (OLR), we deduce pattern speeds and the locations of other resonances.

2. SAMPLE GALAXIES

The four galaxies chosen for this study were selected from the CCD imaging survey of Buta & Crocker (1991, hereafter BC91), who provided images and color index maps of 29 CSRG galaxies containing outer rings or pseudorings. In most of the illustrated cases, the rings belong to the so-called OLR subclasses: R_1 , R'_1 , R'_2 , or $R_1R'_2$. These are the classes where the rings morphologically resemble model outer rings generated near the OLR in test-particle models of barred spirals (e.g., Schwarz 1981; Byrd et al. 1994; Rautiainen et al. 1996). In addition to outer rings, three of the galaxies also have inner rings and two also have a nuclear ring. Positions and classifications from different sources are summarized for each galaxy in Table 1.

NGC 1326 is the brightest of the four. It is illustrated in Figures 4e and 4f of BC91, who detected three rings in the galaxy and a complex dust pattern in the weak bar. The galaxy has an exceptionally strong outer ring of the R_1 variety (meaning it is a true ring, not a pseudoring), with clear dimples near the bar axis, one of the hallmarks of the type. The nuclear ring is also exceptionally strong and is a clear zone of active star formation inside the bar; it has been studied in detail by García-Barretto et al. (1991), Storchi-Bergmann et al. (1996), and Phillips et al. (1996). Triaxial structure inside the ring has been noted by de Vaucouleurs (1974), Buta & Crocker (1993), and Wozniak et al. (1995). The inner ring is distinct but unusual in its relative lack of color contrast. Indeed, the inner ring in this galaxy lacks clear H II regions, which is atypical of most other examples

¹ Department of Physics and Astronomy, University of Alabama, Box 870324, Tuscaloosa, AL 35487-0324.

² Visiting Astronomer, Cerro Tololo Inter-American Observatory, National Optical Astronomy Observatories, operated by the Association of Universities for Research in Astronomy, Inc., under cooperative agreement with the National Science Foundation.

³ Department of Physics and Astronomy, University of Pennsylvania, Philadelphia, PA 19104.

⁴ Department of Physics, Muskingum College, New Concord, OH 43762.

TABLE 1
GLOBAL PHOTOMETRIC CHARACTERISTICS OF SAMPLE GALAXIES

Parameter	NGC 1326	IC 4290	ESO 509-98	ESO 566-24
$\alpha(1950)^a$	03 22 01	13 32 32	13 40 34	09 51 12
$\delta(1950)^a$	-36 38 24	-27 46 00	-25 40 48	-19 20 48
SGC type ^b	(R)SB(r)0 ⁺	SB(r)bc	...	SB(r)b
CSRG type ^c	(R ₁)SB(r)0/a	(R')SB(r)a	(R ₁ R ₂)SB(s)a	(R' ₁)SB(r)b
Carnegie type ^d	RSBa
ESO-B type ^e	S(r)0-a	SB(r)a	S0-a(r)	SB(r)b
log D ₂₅ (0''.1)	1.617 ± 0.005	1.136 ± 0.006	1.100 ± 0.003	1.212 ± 0.004
log R ₂₅	0.157 ± 0.008	0.084 ± 0.009	0.192 ± 0.006	0.138 ± 0.007
ϕ_{25} (1950) (deg)	76.9 ± 0.5	76.6 ± 1.0	37.4 ± 0.2	67.3 ± 0.3
B_T	11.39 ± 0.03	14.19 ± 0.03	14.79 ± 0.03	13.66 ± 0.03
$(U-B)_T$	0.37 ± 0.07	0.31 ± 0.06	0.07 ± 0.06
$(B-V)_T$	0.83 ± 0.04	0.83 ± 0.04	0.90 ± 0.04	0.69 ± 0.04
$(V-I)_T$	1.14 ± 0.04	1.15 ± 0.05	1.18 ± 0.04	1.06 ± 0.04
$(V-R)_T$	0.53 ± 0.04
H_T	7.58 ± 0.04	10.27 ± 0.09	10.73 ± 0.05	9.75 ± 0.05
$(J-H)_T$	0.65 ± 0.07
$(H-K)_T$	0.27 ± 0.05
Photometric axis ratio $\langle q_p \rangle$	0.750 ± 0.002	0.906 ± 0.018	0.640 ± 0.003	0.749 ± 0.006
Photometric major axis $\langle \phi_p \rangle$ (1950) (deg)	73.4 ± 0.5	13.2 ± 4.8	37.9 ± 0.2	69.1 ± 1.0
Radius ranges/Filters for q_p , ϕ_p	145''-165''/R (narrow)	70''-80''/BV	35''-40''/BVI	50''-57''/BVI
Photometric inclination i_p ($q_0 = 0.2 \pm 0.1$) (deg)	42.5 ± 1.1	25.6 ± 2.5	51.6 ± 1.5	42.5 ± 1.2

NOTE.—Units of right ascension are hours, minutes, and seconds, and units of declination are degrees, arcminutes, and arcseconds.

^a de Vaucouleurs et al. 1991.

^b Corwin, de Vaucouleurs, & de Vaucouleurs 1985.

^c Buta 1995.

^d Sandage & Bedke 1994.

^e Lauberts 1982.

studied in detail (see Crocker, Baugus, & Buta 1996, hereafter CBB96). The shape of the bar of the galaxy has been studied by Athanassoula et al. (1990). The galaxy is listed as a LINER by Maia et al. (1987), and is a member of the Fornax Cluster (Maia, da Costa, & Latham 1989).

IC 4290 is a strongly barred spiral with a very bright star-forming inner ring, as shown in Figures 12a and 12b of BC91.⁵ There is no star formation in the inner parts of the bar, which itself is interesting because of its clear boxy character in those regions. The outer pseudoring is one of the faintest known, and could be an R'₁ type. The galaxy was identified as a possible LINER system by Maia et al. (1987).

ESO 509-98 is the prototype of the R₁R'₂ subclass (Buta 1985), a combination of two OLR subclasses that was not predicted to exist by the early test-particle models of Schwarz (1981), which stimulated the production of the CSRG. Although better examples have been identified since 1985 (e.g., NGC 3081, BP98), the galaxy is still an excellent case whose only problem is a small angular size. The galaxy includes an “ansae-type” bar (where the ends of the bar are defined by bright enhancements) and no other rings but the likely OLR features (see Figs. 8e and 8f of BC91). In this sense, it is an excellent case for further study, because the closest any published test-particle models have come to simulating ESO 509-98 is for a high-pattern speed situation where the major resonances inside corotation (CR) are avoided (see Byrd et al. 1994). A new analytic model of ESO 509-98 is presented by Byrd, Ousley, & Dalla Piazza (1998).

ESO 566-24 was presented by BC91 (their Figs. 10a–10d) as the most regular four-armed barred spiral noted in

the CSRG, indeed in the southern sky. The galaxy includes a bright inner ring, a normal bar with linear dust lanes, and a small blue nuclear ring. It has the latest Hubble type (SBb) of our sample.

3. OBSERVATIONS

The optical observations that we will use in this paper are the same as the images presented by BC91. *UBVI* images were obtained with the Cerro Tololo Inter-American Observatory (CTIO) 1.5 m telescope in 1990 February under photometric conditions with a Texas Instruments CCD having a field of view 3.7 square. Based on astrometry, the images were found to have a scale of $0''.547 \pm 0''.001$ pixel⁻¹, and after transposition required a correction of 1.4 ± 0.1 to have 1950 north at the top and east to the left. Flat-fielding was accomplished using a combination of dome flats with a twilight illumination correction. All bias correction, cosmic-ray removal, and flat-fielding was performed with IRAF software.⁶ Transformations to the standard systems were accomplished using standard stars from the catalogs of Landolt (1992) and Graham (1982), and the IRAF PHOTCAL reduction package. Total exposure times and the FWHM of the seeing disk for each filter are listed in Table 2.

In the case of NGC 1326 it was necessary in each filter to mosaic two images offset 60'' to the east and west, in order to have an adequate amount of sky. The mosaics were made using the IRAF routine IMCOMBINE. Since the galaxy still filled most of the mosaic field, we decided to make use of a fairly deep red continuum ($\langle \lambda \rangle = 6477$ Å) image of NGC 1326 obtained by CBB96 to extend our photometry

⁵ Fig. 12a of BC91 incorrectly presents an *I*-band image rather than a *B*-band image. Fig. 13 of the present paper shows a *B*-band image of IC 4290.

⁶ IRAF is distributed by the National Optical Astronomy Observatories, which are operated by the Association of Universities for Research in Astronomy, Inc., under cooperative agreement with the National Science Foundation.

TABLE 2
EXPOSURE TIMES AND SEEING (FWHM)

Filter	NGC 1326 (s, arcsec)	IC 4290 (s, arcsec)	ESO 509-98 (s, arcsec)	ESO 566-24 (s, arcsec)
<i>U</i>	600, 1.62	600, 1.63	600, 1.70
<i>B</i>	480, 1.83	900, 1.59	900, 1.58	1200, 1.75
<i>V</i>	240, 1.84	600, 1.42	1100, 1.56	900, 1.60
<i>R</i> (narrow).....	1200, 1.74
<i>I</i>	180, 1.66	600, 1.46	480, 1.47	480, 1.49
<i>J</i>	500, 2.83
<i>H</i>	1000, 2.28	1200, 2.10	1200, 2.11	1200, 1.97
<i>K</i>	500, 2.39

to the largest possible radii. This image was obtained by CBB96 for a study of H II regions in the galaxy. Although narrowband ($\approx 80 \text{ \AA}$ wide), the image was obtained with a Tektronix 1024×1024 pixel CCD having a field of view of 7.4 square, thus allowing us to better determine the sky level. We refer the reader to CBB96 for the details of these observations. Calibration of this image was obtained using photoelectric Cousins *R*-band multiaperture photometry published by Buta & Crocker (1992, hereafter BC92), and by simulating circular aperture photometry on the array. Although not an exact match to the Cousins *R* band (which involves a very broad filter and usually includes H α emission; see Bessell 1989), the zero point on the *R*-band scale is extremely well-determined, and we will refer to our photometry from this image as *R*-band photometry.

Table 3 summarizes comparisons between published photoelectric aperture photometry of the four galaxies from BC92 and simulated aperture photometry on the arrays. In general, the systematic agreement on optical magnitudes and colors is better than ± 0.05 mag, and we have not made any further corrections to our standard-star zero points. There are problems in specific cases: for IC 4290, the systematic disagreement in *U*–*B* is larger than for ESO 509-98 and ESO 566-24, probably because the signal-to-noise ratio in the *U* band was low in the observations of BC92. For ESO 509-98, BC92 provided measurements in four different apertures, but the largest aperture was greatly affected by bright field stars and the corrected parameters given in BC92 have larger errors. The mean residuals for the field star-corrected measurements in Table 3 exclude this aperture.

Near-infrared images in the Johnson *H* band ($\lambda_{\text{eff}} = 1.65 \mu\text{m}$) were obtained in 1996 February with the Cerro Tololo

Infrared Imager (CIRIM) attached to the CTIO 1.5 m telescope. NGC 1326 was also observed in the Johnson *J* ($\lambda_{\text{eff}} = 1.25 \mu\text{m}$) and *K* ($\lambda_{\text{eff}} = 2.2 \mu\text{m}$) bands. CIRIM is a 256×256 HgCdTe near-infrared camera and multiobject spectrometer 3 array with a field of view of $\approx 5'$ square at $f/7.5$ on the 1.5 m telescope. From astrometry, the scales of the CIRIM images were determined to be $1''.154 \text{ pixel}^{-1}$ in *J*, $1''.142 \text{ pixel}^{-1}$ in *H*, and $1''.139 \text{ pixel}^{-1}$ in *K*. Calibration of the images was made from observations of a few standards from a list by Elias et al. (1982). Further details of the processing of these images are provided by BP98. Table 3 summarizes comparisons between published *JHK* photometry and simulated photometry from our arrays for NGC 1326, the only galaxy in our sample having such photometry available as summarized in the compilation of de Vaucouleurs & Longo (1988). On average, our calibration yields *JHK* magnitudes ≈ 0.1 mag brighter than the published values, a disagreement that is well-determined for the *H* band, since six measurements from two sources were available.

In addition to the above observations, we obtained H α velocity data for three of our sample galaxies with the Rutgers Fabry-Perot interferometer on the CTIO 4 m telescope in 1992 March. Each frame was separated by 1.2 \AA , and the number of frames obtained was 12 for ESO 566-24, eight for IC 4290, and 15 for ESO 509-98. The details of the observations and reduction procedures are the same as discussed in BP98, and will not be repeated here.

4. NEAR-INFRARED MORPHOLOGIES AND COLOR INDEX MAPS

Figure 1 shows the near-infrared morphology of each of the sample galaxies. In general, the rings that are prominent

TABLE 3
COMPARISON OF CCD AND PHOTOELECTRIC APERTURE PHOTOMETRY^a

Galaxy	$\Delta V, \sigma_1, N$	$\Delta(B-V), \sigma_1, N$	$\Delta(U-B), \sigma_1, N$	$\Delta(V-I), \sigma_1, N$	$\Delta J, \sigma_1, N$	$\Delta H, \sigma_1, N$	$\Delta K, \sigma_1, N$
NGC 1326	0.037 0.002 4	0.026 0.007 4	-0.009 0.005 4	0.098 0.016 2	0.100 0.020 6	0.120 0.055 2
IC 4290	0.064 0.056 3	0.031 0.053 3	-0.146 0.068 3	0.010 0.034 3
ESO 509-98.....	-0.045 0.010 4	0.012 0.051 4	0.027 0.058 4	0.046 0.089 4
ESO 566-24.....	0.004 0.015 3	0.000 0.008 3	0.011 0.015 3	0.011 0.010 3

^a Sense of differences is published values *minus* simulated CCD values. σ_1 is the standard deviation, and *N* is the number of measurements compared.

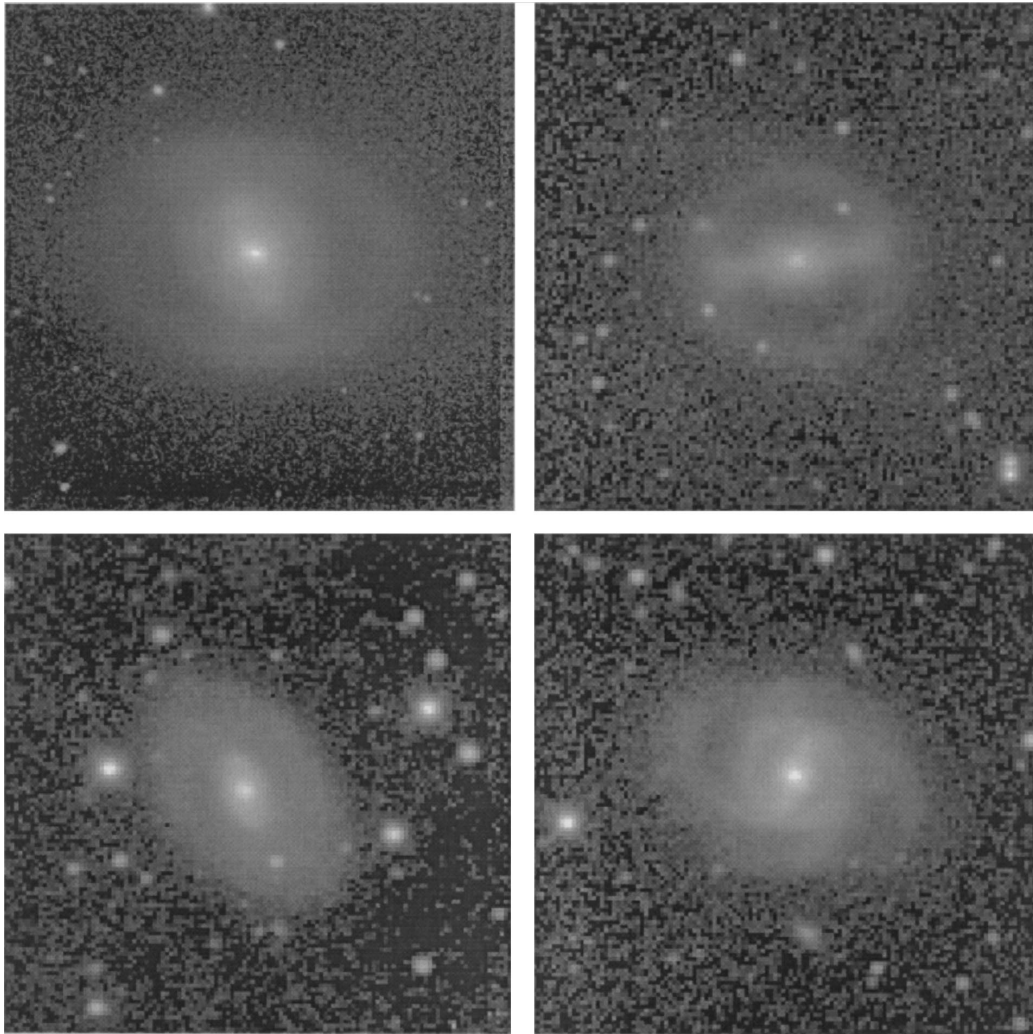


FIG. 1.—Near-infrared (H -band) images of the sample galaxies. *Top left*, NGC 1326; *top right*, IC 4290; *bottom left*, ESO 509-98; *bottom right*, ESO 566-24. The images are in units of mag arcsec^{-2} , ranging from 14.0 to 24.0. The fields shown are 4.8 square for NGC 1326 and 2.4 square for the others, with north at the top and east to the left.

in blue light are still prominent in the near-IR. The outer ring of NGC 1326 and the inner ring of IC 4290 are particularly strong features in the near-IR. As noted in previous studies (e.g., BP98), there is a significant old stellar component underlying the star-forming inner and outer rings of galaxies. In contrast, the prominent nuclear ring in NGC 1326 is not evident in the H band, in spite of the strong star formation seen in optical bands. In this case, there either may be little old stellar component, or the ring has little contrast owing to its location on the steep background light gradient of the bulge. It is also noteworthy that the four-armed spiral pattern in ESO 566-24 that is so prominent in blue light is still clearly seen in the H band.

$B-H$ color index maps are shown for the sample galaxies in Figure 2. The maps are square except for NGC 1326, where the B -band mosaic forces the color index map to be rectangular. The dust in the bar region of NGC 1326 is particularly strong in this color index, which also reveals a blue zone that lies largely beyond the outer ring. Much less color contrast is connected with the inner and outer rings in this galaxy. In IC 4290, the inner ring is a closed oval of star formation somewhat larger than the diameter of the bar, which stands out in the map because of its redder color and lower noise level. The bar of IC 4290 has no offset

dust lanes resolved in our images, as also noted by BC91. In ESO 509-98 and 566-24, blue colors are connected mainly with the spiral arms, but in ESO 566-24 we also see a clear nuclear dust ring associated with leading dust lanes in the bar.

Figure 3 shows a montage of other color index maps for NGC 1326, the only galaxy in our sample for which we can provide near-infrared color maps. All of the maps are seeing-matched and have the same pixel resolution, $1''.142 \text{ pixel}^{-1}$. The two top panels show $B-I$ and $I-H$. Dust is prominent in both color indices, but it is far better emphasized in $B-I$ than in $I-H$. In addition to a very red nucleus, $I-H$ reveals a spot of red colors $\approx 5''$ nearly due west of the center. This spot coincides exactly with a clear break in the nuclear ring seen in both B and $B-I$, and suggests that the break is caused by heavy internal extinction in that section. Interestingly, while the nuclear ring is largely blue in $B-I$, it is slightly red in the near-infrared colors $J-H$ and $H-K$ and is redder than any other regions in the galaxy. This is very similar to what Shaw et al. (1995) and Friedli et al. (1996) have noted for other nuclear rings. The appearance of the ring in these color indices suggests the presence of significant numbers of young M supergiants in the ring.

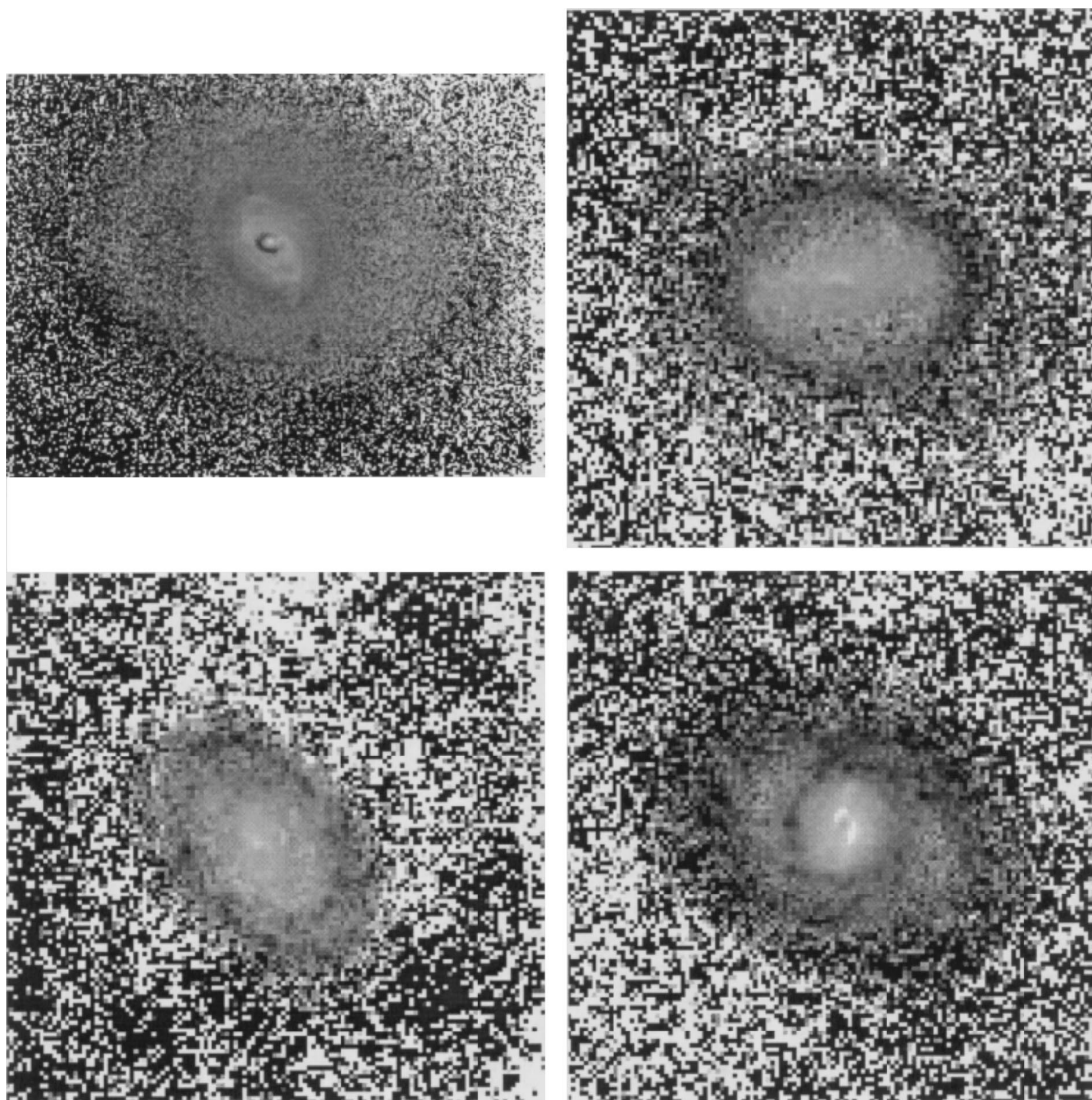


FIG. 2.— $B-H$ color index maps (range 3.0–5.0) of the sample galaxies, showing the distribution of star formation and dust. *Top left*, NGC 1326; *top right*, IC 4290; *bottom left*, ESO 509-98; *bottom right*, ESO 566-24. The gray scale is such that redder features are light while bluer features are dark. The fields shown are 2.4 square for IC 4290, ESO 509-98, and ESO 566-24, and 4.9×3.6 for NGC 1326. In each frame, north is at the top and east is to the left. Note that foreground stars are removed from these images.

The lack of significant star formation associated with the inner and outer rings of NGC 1326 suggests that these features have little gas. Nevertheless, H I gas has been detected from NGC 1326 by Mebold et al. (1979), although these observations did not resolve the location of the gas. It is likely that this gas is associated with the outer blue zone seen in Figure 2, which itself is connected with another ring feature at radii beyond the bright R_1 outer ring (see § 5.2).

5. SURFACE PHOTOMETRY

5.1. Isophotal Analyses and Photometric Orientations

As in previous studies, we have fit ellipses to the isophotes of each of the sample galaxies with the goal of determining the photometric orientation parameters and elliptically averaged luminosity and color profiles. The ellipse fits were made to isophotes of prechosen surface brightness levels using linear least squares, and were in steps of $0.1 \text{ mag arcsec}^{-2}$. Figure 4 shows the results for all four sample galaxies. In this plot, q is the fitted minor axis-to-major axis ratio and ϕ is the fitted position angle reduced to a

1950 coordinate system. Corrections to the raw frame position angles were accomplished via astrometry with standards either from or based on the Space Telescope Science Institute Guide Star Catalog. Only the best images were used for isophote fits. For NGC 1326, the results from the red continuum image only are shown, since this image had the largest field of view of the seven filters used on this galaxy. The dotted horizontal lines in Figure 4 are the adopted mean photometric parameters, listed as $\langle q_p \rangle$ and $\langle \phi_p \rangle$ in Table 1. These means do not refer to a particular isophote in a single filter, but are averages over a range of radii in one or more filters (also given in Table 1) in the outer regions of each galaxy. Also listed in Table 1 are the diameter D_{25} , axis ratio R_{25} , and position angle ϕ_{25} , of the standard B -band isophote having a surface brightness of $\mu_B = 25.00 \text{ mag arcsec}^{-2}$, estimated from ellipse fits.

Table 1 also gives inclination estimates for the galaxies based on $\langle q_p \rangle$ and Hubble's (1926) formula for oblate spheroids using an intrinsic axis ratio $q_0 = 0.2$ (Aaronson, Mould, & Huchra 1980). The table also gives the uncertainty in i provided by an uncertainty of ± 0.1 in this

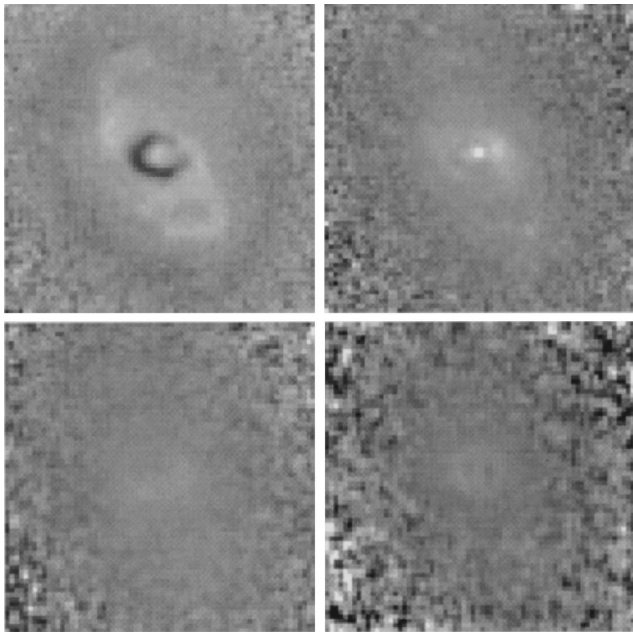


FIG. 3.—Montage of color index maps of NGC 1326. *Top left*, $B-I$ (range 1.0–3.0); *top right*, $I-H$ (range 1.0 to 2.6); *bottom left*, $J-H$ (range 0.15 to 1.25); *bottom right*, $H-K$ (range: -0.20 to 0.80). The gray scale is such that redder features are light while bluer features are dark. The fields shown are 1.3 square in each case, with north at the top and east to the left. Foreground stars are removed from the images.

parameter. The additive correction of $+3^\circ$ advocated by Aaronson et al. (1980) was not applied based on comments by Schommer et al. (1993). An alternative approach to deriving the photometric inclinations would be to use the value of $R_{2.5}$ from Table 1 in conjunction with a type-dependent formula for q_0 , such as that given by Fouqué et al. (1990). This approach gives inclinations of 51° , 37° , 54° , and 45° for NGC 1326, IC 4290, ESO 509-98, and ESO 566-24, respectively. However, as noted by Schommer et al. (1993), use of a single isophote to determine i is more prone to error than use of a mean ellipticity over a range of isophotes in the outer parts of the galaxies. In the cases of NGC 1326 and IC 4290, the inclination value in Table 1 is likely to be more correct.

5.2. Total Magnitudes and Color Indices

With $\langle q_p \rangle$ and $\langle \phi_p \rangle$ to define a fixed ellipse for all the filters obtained on a given galaxy, the elliptically averaged luminosity profiles shown in Figures 5 and 6 were computed. The dashed lines in Figure 5 show how some of the profiles were extrapolated via exponentials to get total magnitudes. For NGC 1326, IC 4290, and ESO 566-24, these exponentials were defined by points in the outer regions and points between the “humps” due to the rings and bars. For ESO 509-98, points beyond $r = 35''$ were used to define an exponential. Integral colors within the largest radii shown for each galaxy were taken to be total colors. Table 1 lists the total magnitudes and colors so derived, the uncertainties given being based on the zero point errors in the standard-star calibrations and estimates of the uncertainty in the sky level. The optical parameters agree very well with the values obtained by BC92 based on growth-curve fits to photoelectric multiaperture photometry, except for $U-B$ for IC 4290, as discussed previously. Our total I -band magnitude for NGC 1326, $I_T = 9.42 \pm 0.03$, agrees well with the

value (9.47 ± 0.02) obtained by Bureau, Mould, & Staveley-Smith (1996).

In general, the luminosity profiles of these galaxies are very complex, with strong bumps due to the rings and/or spiral structure. The most distinctive profile is seen in ESO 509-98 (Fig. 5, *lower left panel*), where the average profile is uniform over a significant range in radius. Outside this plateau, which is very like what is commonly referred to as a “lens” (Kormendy 1979), the luminosity gradient is very steep compared with the other three objects. It is not possible to determine whether the exponential decline beyond $35''$ seen in ESO 509-98 continues to significantly larger radii than $60''$. The extended plateau is blue, as indicated by the $B-H$ color index profile (see Fig. 6, *lower left panel*), and less uniform in the near-IR.

The exponentially declining average backgrounds shown in Figure 5 can be used to bring out weak details not clearly distinguishable in the raw images of these galaxies. In the case of NGC 1326, subtraction of the exponential in Figure 5 in two dimensions from the red continuum image reveals the existence of an extremely low surface brightness, fourth ring feature, shown in the left panel of Figure 7. The ring has a major-axis radius of $132''$, an axis ratio of 0.84, and a major-axis position angle of 70° . On the east side, this feature appears to connect to the R_1 ring via spiral structure, which suggests that it may be an R'_2 outer pseudoring similar to that seen in NGC 3081 by BP98. The feature seems well-separated from the R_1 , unlike in NGC 3081, where the R_1 and R'_2 features nearly intersect.

In the case of ESO 566-24, subtraction of the exponential background shown in Figure 5 reveals a faint ringlike feature enveloping the four-armed spiral zone (see Fig. 7, *right panel*). Unlike the feature in NGC 1326, this faint ring in ESO 566-24 cannot be fitted easily into a particular morphological resonance ring category.

5.3. Integral Colors of Features

The rings in NGC 1326 and IC 4290 are well-defined features whose colors can be measured in an integral sense by defining elliptical annuli whose shapes, widths, and orientations are similar to the apparent shapes, widths, and orientations of the features. This will provide some quantitative information on the stellar populations that define such features. Similar data are provided for NGC 3081 by BP98.

Table 4 provides the integrated information for the three main rings of NGC 1326 and the bar and inner ring of IC 4290. The notes to the table summarize the parameters of the elliptical annuli used to define the features. These parameters are based on visual mappings of the features on the B -band images, and hence are indicative rather than definitive. The colors listed are as observed. According to de Vaucouleurs et al. (1991), the Galactic extinctions toward NGC 1326 and IC 4290 are $A_B(G) = 0.00$ and 0.21 mag, respectively. Using Table 3 and equations (3a) and (3b) from Cardelli, Clayton, & Mathis (1989), the Galactic reddening corrections to the colors of IC 4290 are $E(U-B) = 0.04$ mag, $E(B-V) = 0.05$ mag, and $E(V-I) = 0.06$ mag. Internal extinction corrections are much more difficult to assess and will not be considered, but K corrections could be applied according to standard procedures (de Vaucouleurs et al. 1991). A useful comparison between the corrected colors of the inner and outer rings of NGC 1326 and the bar and inner ring of IC 4290 is provided by the synthetic

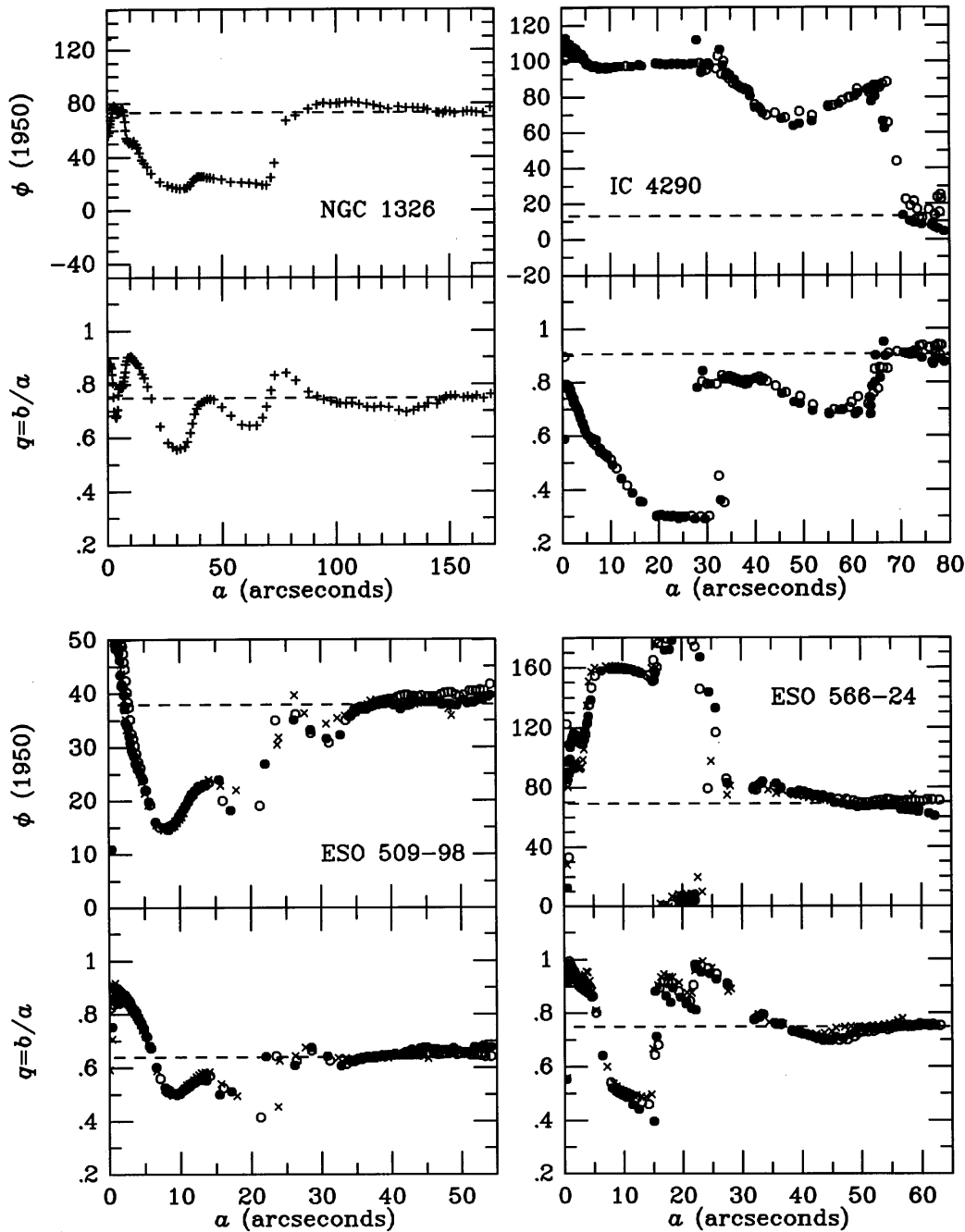


FIG. 4.—Results of ellipse fits to optical isophotes of the sample galaxies. Filled circles represent B , open circles represent V , crosses represent I , and pluses represent red-continuum results. The parameter q is the fitted minor axis-to-major axis ratio. The position angles ϕ have been reduced to a 1950 coordinate system.

galaxy colors computed by Kennicutt, Tamblyn, & Congdon (1994). The colors of these features fit well into the synthetic colors computed for a Salpeter Initial Mass Function and a 10^{10} yr-old stellar system. The model assumes an exponential star formation history with e -folding time τ and birthrate parameter b (defined as the star formation rate at present relative to the average past star formation rate). The $B-V$, $V-R$, and $V-I$ colors of the inner ring of NGC 1326 imply a $\langle\tau\rangle$ of 2 ± 0.5 Gyr and $\langle b\rangle$ of 0.04 ± 0.03 , while those for the outer ring imply a $\langle\tau\rangle$ of 1.4 ± 0.5 and $\langle b\rangle$ of 0.02 ± 0.02 . Similar calculations for the nuclear ring would not be useful, because internal extinction is obviously important in that region. For IC 4290, the corrected colors of the inner ring imply $\langle\tau\rangle = 3.5 \pm 0.4$ and

$\langle b\rangle = 0.17 \pm 0.04$, while those for the bar imply $\langle\tau\rangle < 1$ and $\langle b\rangle < 0.0005$. The colors of the three ring features considered are consistent with models of declining star formation rates with rather low current rates. The colors of the bar of IC 4290 are consistent with a region composed entirely of old stars.

6. FABRY-PEROT INTERFEROMETRY

6.1. H II Region and Radial Velocity Distributions

The Fabry-Perot interferometry provided kinematic and H II region information for three of our sample galaxies: IC 4290, ESO 509-98, and ESO 566-24. Fortunately, an H α map of NGC 1326 is available from CBB96, so that only the

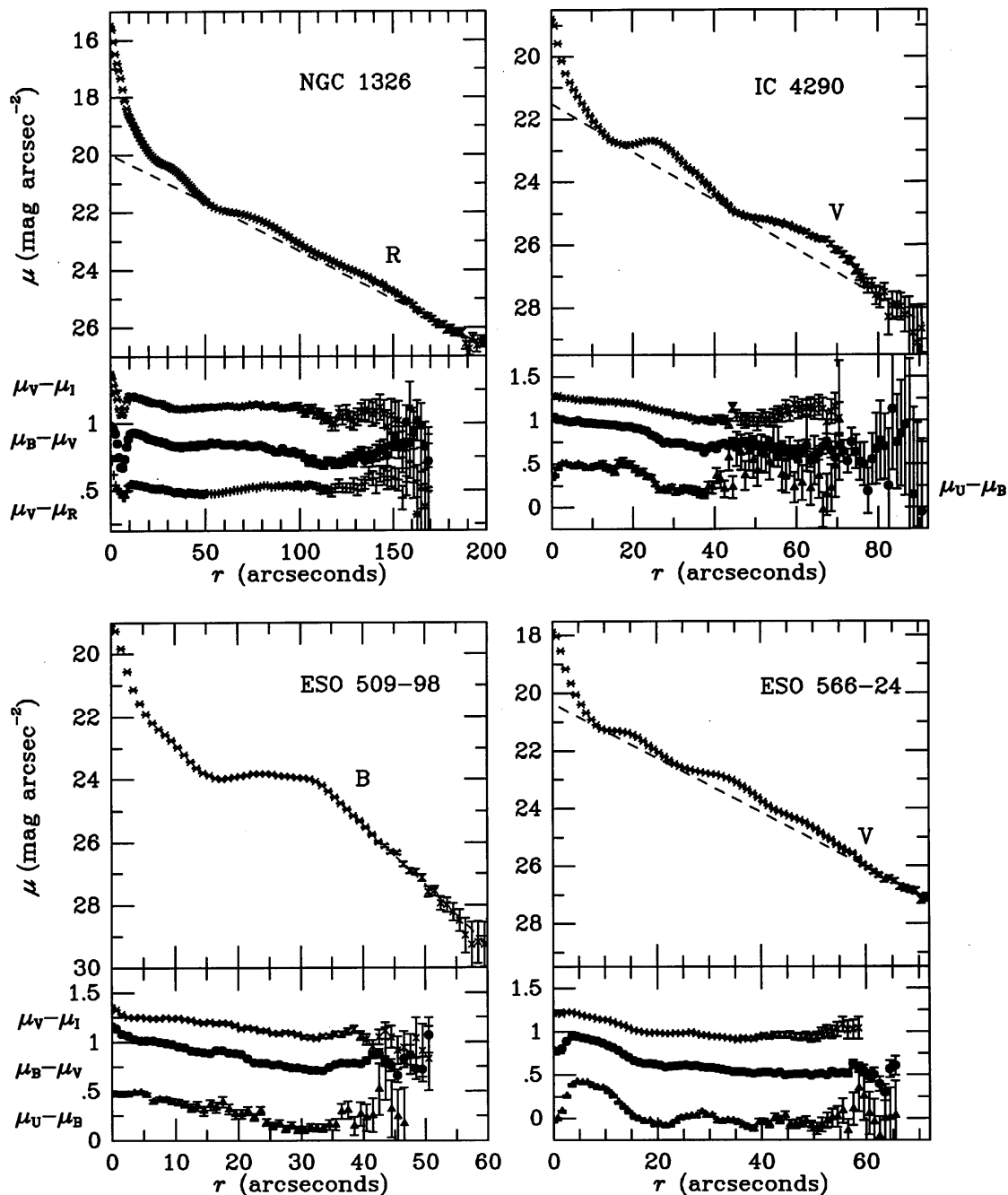


FIG. 5.—Elliptically averaged optical surface brightness and color index profiles of the sample galaxies. Error bars are based on the gain and readnoise of the detector, photon counting statistics, and estimated errors in the determination of the sky level. For NGC 1326, IC 4290, and ESO 566-24, the dashed lines are exponential representations of the background light underlying the humps in the profiles.

velocity field is missing for this galaxy. However, some information on the rotation velocities in NGC 1326 is provided by Storchi-Bergmann et al. (1996). In general, Fabry-Perot interferometry provides four maps of a given galaxy: the emission-line map, the velocity field, the velocity dispersion map, and the continuum map. Here we will illustrate only the first two types of maps.

Figure 8 shows the emission-line maps of the three observed galaxies. In IC 4290, most of the H II regions are confined to the bright inner ring, with very few in the bar region or outside the ring. There is a nuclear source of emission and also an H II region close to the center. In ESO 566-24, the inner ring is a bright concentration of H II regions, but there are also plenty of H II regions connected

with the outer spiral arms. Although the four-armed pattern is very prominent in blue light, it is barely recognizable in H α emission. A significant fraction of the H α flux from ESO 566-24 comes from the bright central region, where a nuclear ring was noted by BC91. The nuclear H α emission is not, however, ringlike. In ESO 509-98, we see H II regions mainly connected with the strong R $_2$ feature and virtually no central emission.

The distribution of H II regions in NGC 1326 is described by CBB96, who noted the absence of any H II regions connected with the inner ring or the ridge-line of the outer ring. Most of the emission comes from the vicinity of the bright nuclear ring. For unknown reasons, there is a concentration of H II regions in the southern half of the bar, and virtually

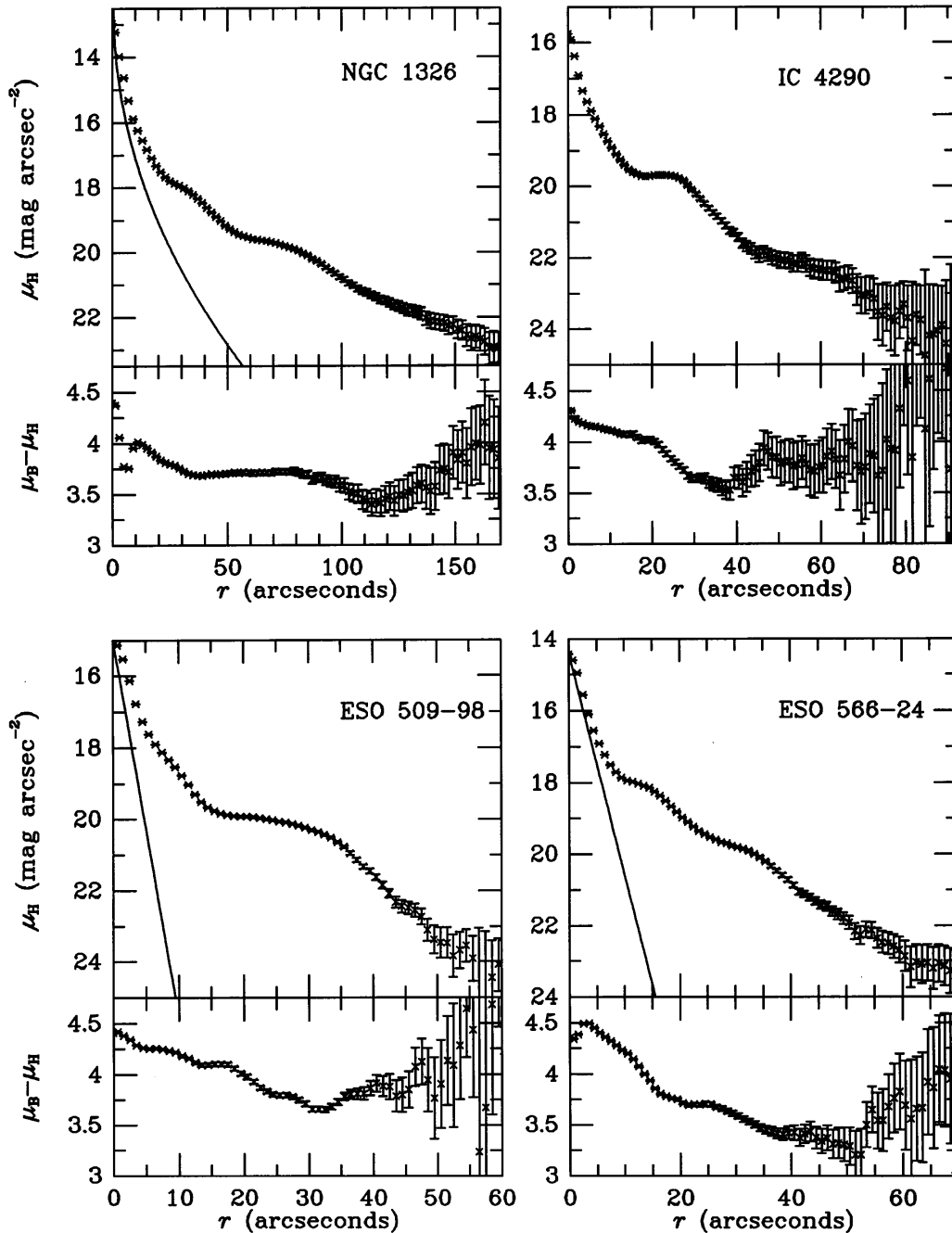


FIG. 6.—Elliptically averaged H -band surface brightness and $B-H$ color index profiles of the sample galaxies. Error bars are based on the gain and readnoise of the detector, photon counting statistics, and estimated errors in the determination of the sky level. The solid curves show the adopted bulge models for three of the galaxies. Note that in the elliptically averaged profiles, the parts of the profiles where the bulge dominates are distorted by the averaging ellipses, which represent the projected disk shape only.

all outer $H\ II$ regions follow a two-armed spiral pattern beyond the ridge-line of the R_1 outer ring (see § 7).

6.2. Velocity Fields

The velocity fields of the three observed galaxies are shown in Figure 9. In IC 4290, the kinematic line of nodes clearly differs from the position angle of the inner-ring major axis, indicating that this feature is likely to be intrinsically elongated. The velocity field of ESO 566-24 brings to light the presence of a likely physical companion. There is a small zone of discrepant velocities (compared with neighboring pixels) $24''$ due west of the center of the galaxy. This zone coincides with a small diffuse object seen in Figure 10a

of BC91. Figure 10c of BC91 shows that this diffuse object is blue and may be a star-forming dwarf companion of ESO 566-24. In spite of the similar radial velocities, it is not likely that the two galaxies are seriously interacting: ESO 566-24 has remarkable symmetry, and indeed is the most symmetric four-armed barred spiral yet identified. In ESO 509-98, the kinematic line of nodes closely approximates the major-axis position angle of the R_2' feature.

6.3. Rotation Curves and Kinematic Orientation Parameters

The kinematic parameters of IC 4290, ESO 509-98, and ESO 566-24 were derived using mainly two approaches: the

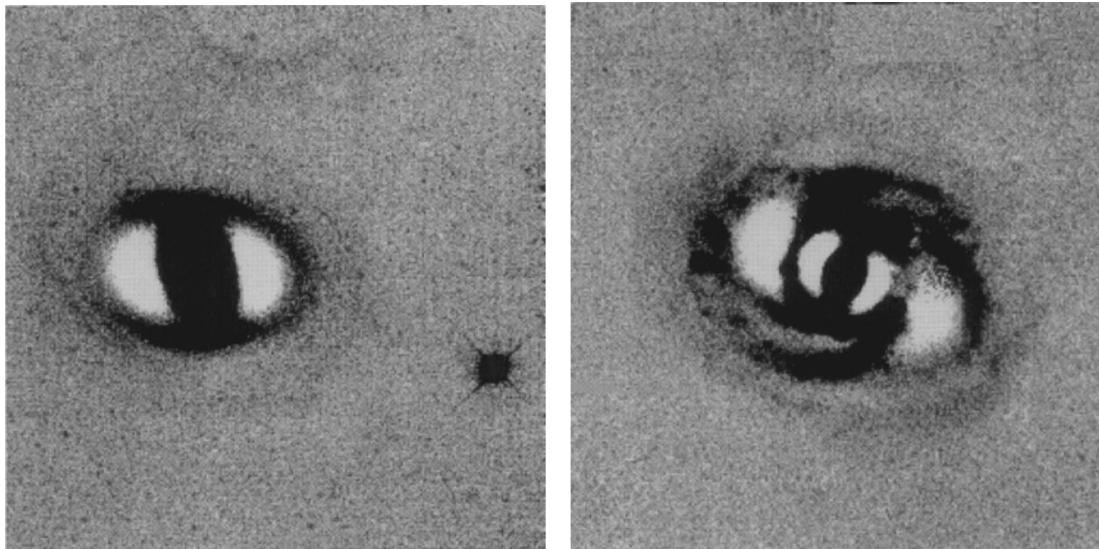


FIG. 7.—*Left*: Red continuum image of NGC 1326 after subtraction of an underlying exponential disk model. This reveals a fourth faint ring in the outermost parts of the disk. The field shown is 7.4 square. *Right*: B-band image of ESO 566-24 after subtraction of an underlying exponential disk model. A faint partial ring is revealed beyond the main four-armed pattern. The field shown is 2.3 square. North is at the top and east is to the left.

method of Warner, Wright, & Baldwin (1973), which iterates for the rotation center, the heliocentric systemic velocity, the inclination, and the line of nodes by minimizing the residuals of the deprojected circular velocity; and the method of van Moorsel & Wells (1985), which fits a projected model velocity field based on a parametrized rotation curve. Table 5 summarizes our best judgments of the systemic velocity, line of nodes position angle, and inclination from these methods, including the uncertainties in the estimated parameters. The kinematic inclinations are poorly determined for IC 4290 and ESO 566-24. In all three cases, the rotation center was found to be within uncertainties coincident with the continuum nucleus.

The distances Δ for the sample galaxies were determined as follows: For NGC 1326, we used the *I*-band Tully-Fisher distance of the Fornax Cluster, 15.4 ± 2.3 Mpc, obtained by Bureau et al. (1996). For the other three galaxies, the distances were computed using the measured systemic velocities and the linear Virgocentric flow model (Aaronson et al. 1982). This method only gives distances relative to the distance of the Virgo Cluster. Ferrarese et al. (1996) obtained a distance of 16.1 ± 1.3 Mpc for M100, a bright Virgo Cluster spiral, based on *Hubble Space Telescope* observations of

Cepheid variables, while Sandage & Tammann (1995) obtained 21.3 ± 2.7 Mpc, based on globular cluster luminosity functions. D’Onofrio et al. (1997) obtained a relative distance modulus of 0.45 ± 0.15 mag between the Virgo and Fornax Clusters from D_n, σ and Fundamental Plane techniques, which would correspond to 18.9 ± 2.5 Mpc using the Bureau et al. (1996) distance to Fornax. Pierce, McClure, & Racine (1992) obtained a distance of 15.1 ± 1.4 Mpc to Virgo Cluster spiral NGC 4571 from the magnitudes of brightest supergiants. Gonzalez & Faber (1997) favor an unbiased estimate of 17.2–17.4 Mpc for the distance to the Virgo Cluster, while Fouqué et al (1990) derived what they considered to be an unbiased distance of 19 ± 2 Mpc. We adopt $\Delta_{\text{Virgo}} = 17 \pm 2$ Mpc, which leads to the distances for our galaxies given on the bottom line of Table 5.

We can now compare the kinematic orientation parameters with the measured photometric values. For ESO 509-98, the photometric major-axis position angle differs by 3° from the kinematic line of nodes position angle. The kinematics also favor an inclination 3° larger than the photometric value. For an object with an inclination greater than 50° , these are typical disagreements (Schommer et al. 1993).

TABLE 4
INTEGRATED COLORS OF FEATURES IN NGC 1326 AND IC 4290

Galaxy	Feature	<i>B</i> – <i>V</i>	<i>U</i> – <i>B</i>	<i>V</i> – <i>R</i>	<i>V</i> – <i>I</i>	<i>J</i> – <i>H</i>	<i>H</i> – <i>K</i>	<i>B</i> – <i>H</i>	Notes
NGC 1326.....	Nuclear ring	0.70	...	0.49	1.08	0.68	0.28	3.75	a
m.e.:		0.03	...	0.03	0.03	0.06	0.03	0.03	a
NGC 1326.....	Inner ring	0.82	...	0.49	1.10	0.64	0.21	3.67	b
m.e.:		0.03	...	0.03	0.03	0.06	0.03	0.03	b
NGC 1326.....	Outer R_1 ring	0.82	...	0.53	1.13	0.63	0.25	3.70	c
m.e.:		0.03	...	0.03	0.03	0.07	0.04	0.04	c
IC 4290	Bar	0.98	0.51	...	1.24	4.14	d
m.e.:		0.03	0.05	...	0.03	0.03	d
IC 4290	Inner ring	0.73	0.19	...	1.06	3.62	e
m.e.:		0.03	0.05	...	0.03	0.03	e

^a Defined by an elliptical annulus having $3^\circ 95' \leq a \leq 6^\circ 45'$, $\phi(1950) = 91^\circ$, $q = 0.75$.
^b Defined by an elliptical annulus having $30^\circ 2' \leq a \leq 37^\circ 2'$, $\phi(1950) = 40^\circ$, $q = 0.77$.
^c Defined by an elliptical annulus having $77^\circ 0' \leq a \leq 97^\circ 0'$, $\phi(1950) = 87^\circ$, $q = 0.63$.
^d Defined by an elliptical annulus having $5^\circ 0' \leq a \leq 24^\circ 0'$, $\phi(1950) = 99^\circ$, $q = 0.29$.
^e Defined by an elliptical annulus having $25^\circ 7' \leq a \leq 33^\circ 7'$, $\phi(1950) = 97^\circ$, $q = 0.84$.

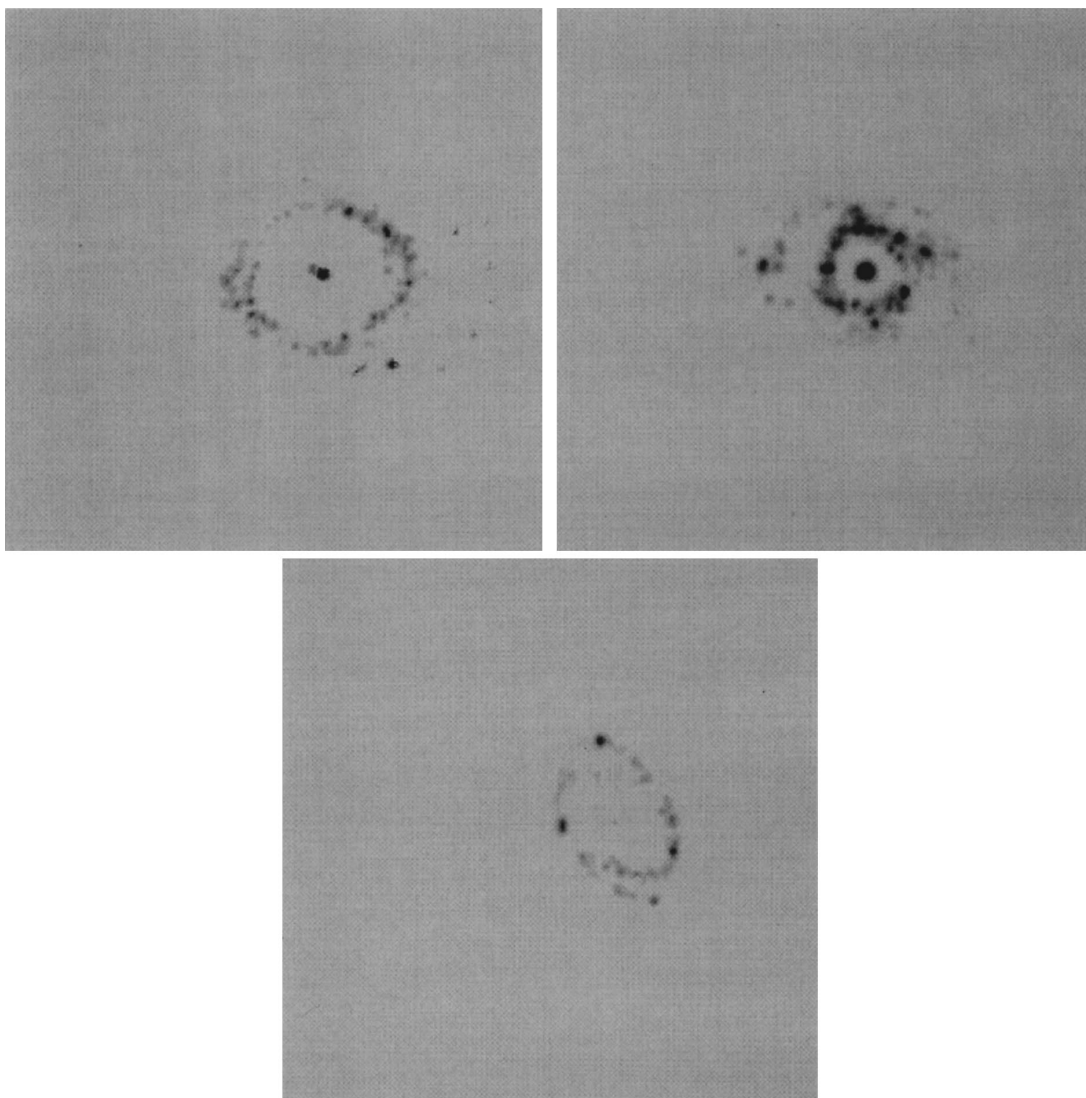


FIG. 8.—Distribution of H II regions in three sample galaxies from Fabry-Perot interferometry. The panels are IC 4290 (*top left*), ESO 566-24 (*top right*), and ESO 509-98 (*bottom*). The fields shown are 3:3 square in each case. North is at the top and east is to the left.

In the case of IC 4290, the photometric major-axis position angle differs from the kinematic line of nodes position angle by 36° , a sure sign of a low inclination. The kinematic inclination is an uncertain $20^\circ \pm 10^\circ$, compared with the photometric value of 26° . Since the small difference in these values can have a large impact on the maximum rotation velocity, we used the *I*-band Tully-Fisher relation (Pierce & Tully 1992) to make a third estimate of the inclination by determining what inclination would be needed to place IC 4290 at its redshift distance of 62 ± 7 Mpc given its observed velocity field. This yielded an estimate of $22^\circ \pm 2^\circ$,

intermediate between the photometric and kinematic values. We adopt this value, but the indicated uncertainty does not include the uncertainty involved in applying a Tully-Fisher relation based mainly on galaxies inclined more than 45° .

For ESO 566-24, the photometric major axis position angle is 4° less than the kinematic value, while the photometric inclination is 8° greater than the kinematic value. The shapes of outer isophotes of ESO 566-24 clearly do not support an inclination as low as 35° for this galaxy. We suspect that the orientation of the system, with the bar lying nearly perpendicular to the line of nodes, causes noncircular motions to mimic a lower inclination velocity field. Use of the Pierce & Tully (1992) Tully-Fisher relation for the total *I*-band magnitude of ESO 566-24 also favors the photometric inclination, giving a distance of 52 Mpc compared with the redshift value of 45 ± 5 Mpc. The kinematic inclination gives a distance of 71 Mpc.

For NGC 1326, Storchi-Bergmann et al. (1996) deduced a kinematic line of nodes position angle of $81^\circ \pm 3^\circ$ from three-slit spectra in a position angle of 77° . This differs from our photometric value of 73.4° based on the deep red contin-

TABLE 5
KINEMATIC PARAMETERS OF SAMPLE GALAXIES

Parameter	IC 4290	ESO 509-98	ESO 566-24
V_s (km s $^{-1}$)	4810 ± 3	7983 ± 3	3492 ± 3
ϕ_k (receding) (deg).....	49 ± 3	35 ± 1	73 ± 1
i_k (deg).....	20 ± 10	55 ± 2	35 ± 5
Δ (Mpc)	62 ± 7	101 ± 12	45 ± 5

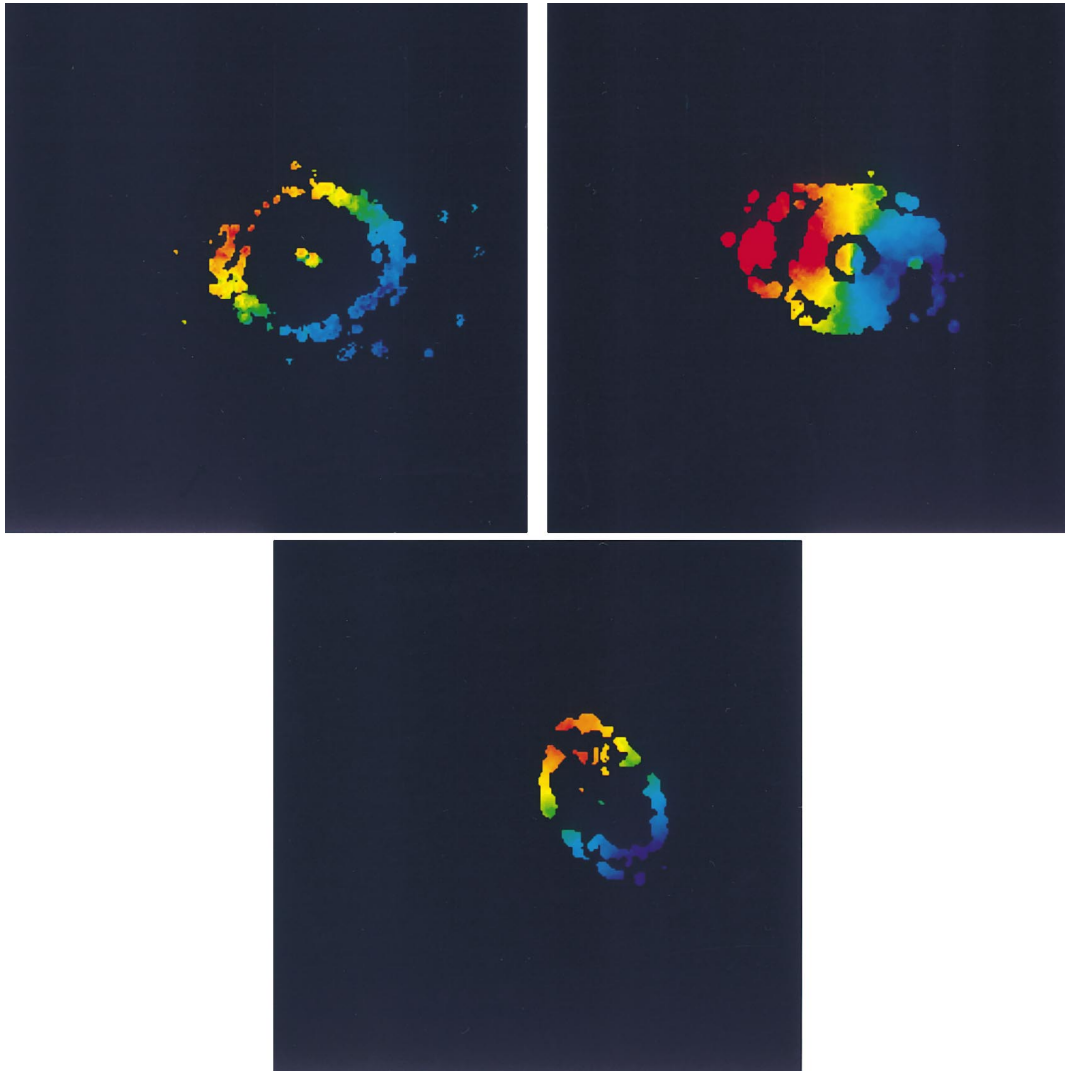


FIG. 9.—Velocity fields of three sample galaxies from Fabry-Perot interferometry. The panels and velocity ranges (blue to red) are as follows: *Top left*, IC 4290, 4600–5000 km s⁻¹; *top right*, ESO 566-24, 3200–3800 km s⁻¹; *bottom*, ESO 509-98, 7500–8500 km s⁻¹. The fields shown are 3:3 square in each case. North is at the top and east is to the left. In the map for ESO 566-24, the spot of apparently discrepant velocities 24" due west of the center is due to a small companion galaxy.

uum image. Because Storchi-Bergmann et al.'s measurements cover only a very limited number of points around and in the nuclear ring, it is difficult to evaluate the significance of this difference. Tentatively, we will adopt the photometric major axis to be the line of nodes of the galaxy.

The case of IC 4290 illustrates how simple averages of the photometric and kinematic orientation parameters may not be appropriate for our sample galaxies where both sets of parameters are available. As for NGC 3081 (BP98), we have decided instead to adopt the kinematic line of nodes position angles for the remainder of our analyses of IC 4290, ESO 509-98, and ESO 566-24, but have favored the photometric or Tully-Fisher inclinations over the kinematic inclinations, given the sparse coverage of the measured velocity fields. Figure 10 illustrates the unfolded rotation curves of these galaxies based on velocity points within $\pm 45^\circ$ of the line of nodes. For the most part, the rotation curves are very normal-looking. Excellent symmetry is observed for ESO 566-24, which shows a normal flat rotation curve, while for ESO 509-98 the rotation velocity is constant on one side, slightly rising on the other. For IC 4290, there is a suggestion of a slight decrease in rotation velocity at larger radii.

Maximum rotation velocities, averaged over both halves of the major axis, are $V_m = 197 \pm 3$, 259 ± 1 , and 198 ± 1 km s⁻¹ for IC 4290, ESO 509-98, and ESO 566-24, respectively.

7. DEPROJECTED STRUCTURE OF THE GALAXIES

One of the main goals of this study is to evaluate the results of statistics concerning the shapes and bar alignments of galactic rings. Using large samples of apparent axis ratios and relative bar/ring position angles from the CSRG, Buta (1995) deduced that inner rings in SB galaxies have an average intrinsic axis ratio of 0.81 ± 0.06 and are aligned parallel to the bar axis, while outer rings may be aligned parallel or perpendicular to the bar axis with an average intrinsic axis ratio of 0.82 ± 0.07 . We ask whether the galaxies in our small sample provide any independent support for these statistical results, realizing that individual cases may depart significantly from the mean characteristics.

To deproject the galaxies, we used IRAF routine IMLIN-TRAN, assuming the material of interest (in the rings) is confined largely to a thin disk. For our main analysis, we have used the orientation parameters applied to the rota-

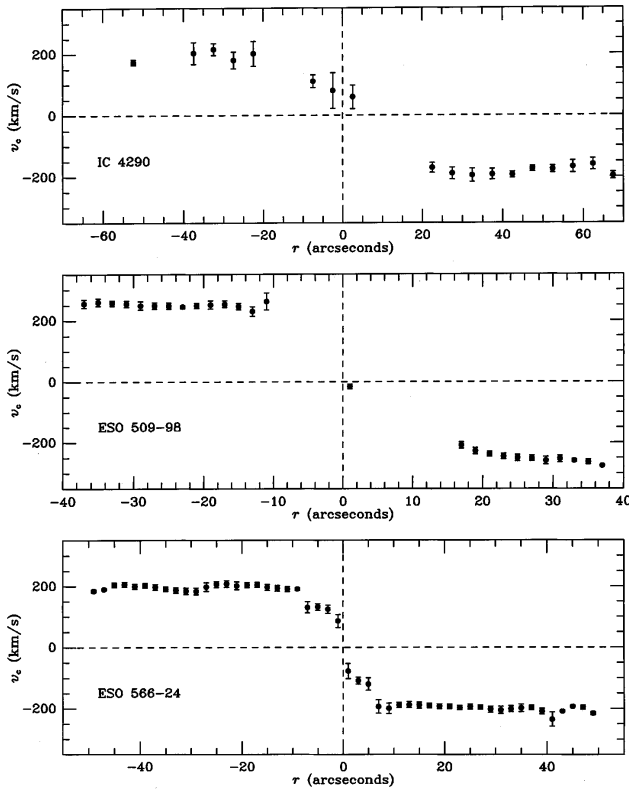


FIG. 10.—Unfolded rotation curves of three sample galaxies from Fabry-Perot interferometry. The inclinations i and line of nodes position angles ϕ_n used for these curves are 22° , 49° for IC 4290; 52° , 35° for ESO 509-98; and 43° , 73° for ESO 566-24. Positive radii are to the southwest and negative radii are to the northeast in each case. Error bars are 1σ standard deviations about the means.

tion curve analyses for IC 4290, ESO 509-98, and ESO 566-24 (i.e., the kinematic line of nodes position angle in conjunction with the photometric or Tully-Fisher inclination), while for NGC 1326 we used only the photometric major-axis position angle and inclination. In each case, after deprojecting the galaxy, we rotated the image so that the bar is horizontal, with the deprojected bar position

angle being based on the H -band image where it is least affected by dust. Note that these are not expected to be accurate deprojections, since the actual three-dimensional light distribution is not known for any of these galaxies. Also, the deprojections described in this section were made in the B band mainly, but since no decompositions of the bulge were made in this filter, the bulges are somewhat stretched in the deprojected images. In addition to the adopted orientation parameters, we also deprojected each galaxy for an alternative set of parameters to judge the reliability of some of our deductions. These are discussed further below.

Figure 11 shows the deprojected B -band mosaic of NGC 1326. Here we see the classic morphology of perpendicularly aligned inner and outer rings with the inner ring aligned parallel to the bar. The appearance of NGC 1326 in this image is very similar to that for NGC 3081, only the outer ring of NGC 1326 deprojects to a somewhat rounder shape. Using a cursor and a monitor, we visually mapped the deprojected ridge-lines of the four rings in NGC 1326, and then fit ellipses to the points. The results are summarized in Table 6, which gives the relative bar/ring major-axis position angle θ_{Br} , the fitted semimajor-axis diameter a , and the fitted minor axis-to-major axis ratio q . In spite of the weak bar, the deprojected axis ratio, 0.69, of the inner ring of this galaxy (for the adopted orientation parameters of $i = 43^\circ$, $\phi_n = 73^\circ$) is considerably less than the statistical average for SB inner rings, but comparable to that found for the inner ring of NGC 3081. The deprojected axis ratio of the outer R_1 ring, 0.83, is comparable to the mean intrinsic outer ring axis ratio for SB galaxies, but rounder than the average R_1 ring in the CSRG. The alignments are consistent with CSRG statistics. The nuclear ring deprojects into a relatively round feature misaligned with the primary bar, as is also typical (Buta & Crocker 1993). The probable R_2 feature deprojects into a feature having an axis ratio of 0.88 misaligned with the bar axis by 18° . The misalignment may not be very significant, given the extreme faintness of the feature and the location of the galaxy in the Fornax Cluster.

Figure 12 shows the distribution of H II regions in NGC 1326 as superposed on the deprojected ellipse fits to the

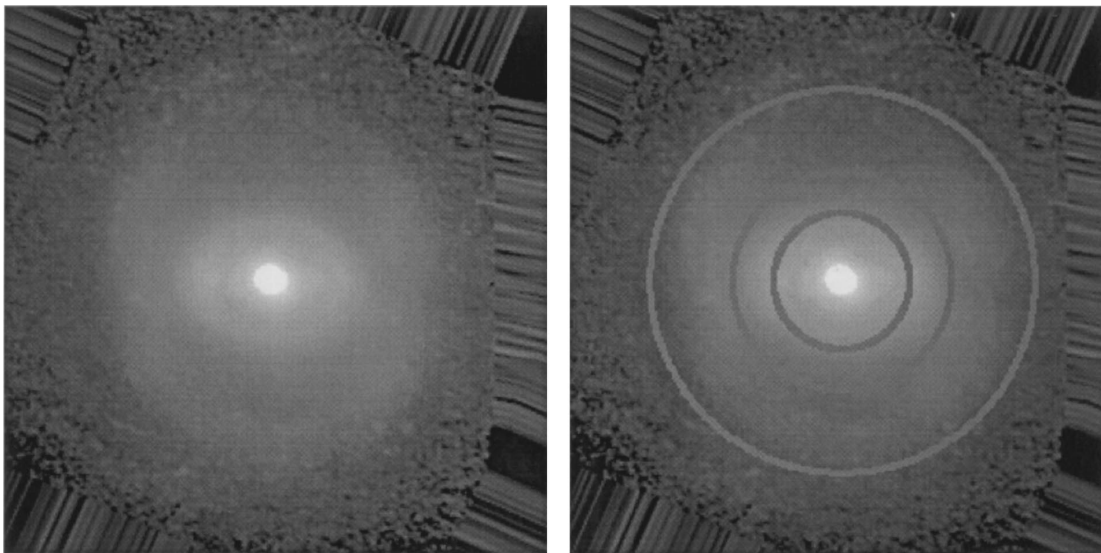


FIG. 11.—*Left*: Deprojected B -band image of NGC 1326. Note the near perpendicular alignment of the inner and outer rings. *Right*: same image, with resonance circles UHR (*innermost*), CR, and OLR (*outermost*) superposed.

TABLE 6
RESULTS OF FITS TO DEPROJECTED RINGS

Object	i, ϕ_n (deg)	Feature	Filter	θ_{Br} (deg)	a (arcsec)	q
NGC 1326	43, 73	Nuclear ring	$B-H$	67	6.7	0.87
NGC 1326	48, 81	Nuclear ring	$B-H$	34	6.8	0.91
NGC 1326	43, 73	Inner ring	B	1.8	43	0.69
NGC 1326	48, 81	Inner ring	B	0.7	48	0.60
NGC 1326	43, 73	R_1 outer ring	B	86	92	0.83
NGC 1326	48, 81	R_1 outer ring	B	84	90	0.95
NGC 1326	43, 73	R_2 outer ring	B	18	150	0.88
NGC 1326	48, 81	R_2 outer ring	B	8	167	0.78
IC 4290	22, 49	Inner ring	B	0.5	31	0.81
IC 4290	26, 13	Inner ring	B	3.7	33	0.74
IC 4290	22, 49	Inner ring	H	18	26	0.98
IC 4290	26, 13	Inner ring	H	12	28	0.89
IC 4290	22, 49	Outer pseudoring	B	77	70	0.75
IC 4290	26, 13	Outer pseudoring	B	84	67	0.83
ESO 509-98	52, 35	R_1 outer ring	B	90	25	0.87
ESO 509-98	55, 38	R_1 outer ring	B	73	26	0.89
ESO 509-98	52, 35	R_2 outer ring	B	19	33	0.93
ESO 509-98	55, 38	R_2 outer ring	B	13	35	0.89
ESO 566-24	43, 73	Inner ring	B	5.1	19	0.74
ESO 566-24	35, 69	Inner ring	B	6.5	17	0.83
ESO 566-24	43, 73	Faint outer ring	B	3.9	50	0.94
ESO 566-24	35, 69	Faint outer ring	B	63	47	0.94

rings. This shows that, except for the bar and nuclear ring, the H II regions in this galaxy lie between the two outer rings.

Table 6 also lists the results of fits to the rings of NGC 1326 using the orientation parameters, $i = 48^\circ$, $\phi_n = 81^\circ$, derived by Storchi-Bergmann et al. (1996). With these parameters, the near-perpendicular relative orientation of the inner and outer rings is still present, but the inner ring would be much more elongated and the outer ring much rounder, than for our adopted orientation parameters.

Deprojected B -band images of IC 4290 are shown in Figure 13, and the results of visual mappings of the ring

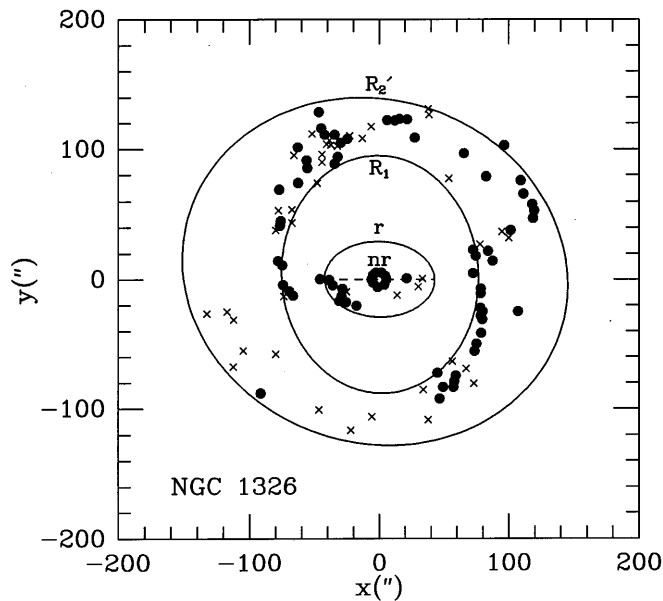


FIG. 12.—Graph showing the deprojected distribution of H II regions in NGC 1326 relative to the ridge-lines of its four ring features. Solid curves represent ellipses fitted to visual mappings of the rings, where “nr” corresponds to the nuclear ring, “r” to the inner ring, and “ R_1 ” and “ R_2 ” to the outer rings. Filled circles represent the brighter H II regions, while crosses represent fainter ones. Note how most H II regions lie between the two outer rings.

features are summarized in Table 6. In blue light, and for the adopted orientation parameters of $i = 22^\circ$, $\phi_n = 49^\circ$, the inner ring deprojects into an oval having an axis ratio of 0.81 and an alignment parallel to the bar, consistent with the mean for SB inner rings from CSRG statistics. In the H band, the deprojected inner ring looks much rounder in shape. The impression is partly subjective, but seems connected with the more spiral appearance of the inner ring in blue light, such that its major axis is underfilled by the bar. The spiral character of the ring is less evident in the H band. We have also visually mapped the appearance of the deprojected faint outer pseudoring of the galaxy. Ignoring the obvious arm-doubling on the right side of the image, this feature is 2.2 times the diameter of the inner ring, has an axis ratio of 0.75, and is aligned 77° to the bar axis. It could be an R_1 -type pseudoring, but it is made of spiral arms that wind nearly 360° , rather than the usual 180° .

Table 6 also presents the results of fits to the rings of IC 4290 using the photometric major-axis position angle and the photometric inclination. In spite of the drastically different line of nodes position angle, the alignment of the inner ring along the bar axis is still preserved, owing to the low inclination.

The deprojected B -band image of ESO 566-24 is shown in Figure 14. As for NGC 1326 and IC 4290, the inner ring deprojects into an oval aligned parallel to the bar axis. The results of a visual mapping are summarized in Table 6. In this case, the intrinsic axis ratio, for the adopted orientation parameters of $i = 43^\circ$, $\phi_n = 73^\circ$, is 0.74, slightly less than the CSRG mean for SB inner rings. The four outer arms of ESO 566-24 deproject into a spectacular circular zone reminiscent of the logo of the Samsonite Corporation. As is also shown in Table 6, use of the photometric major-axis position angle and the kinematic inclination as alternatives to our adopted values preserves the alignment of the inner ring along the bar but makes it less elongated.

The deprojected B -band image of ESO 509-98 is shown in Figure 15. In this case, the deprojection helps to highlight some slight asymmetry in the outer regions of the R_2 feature

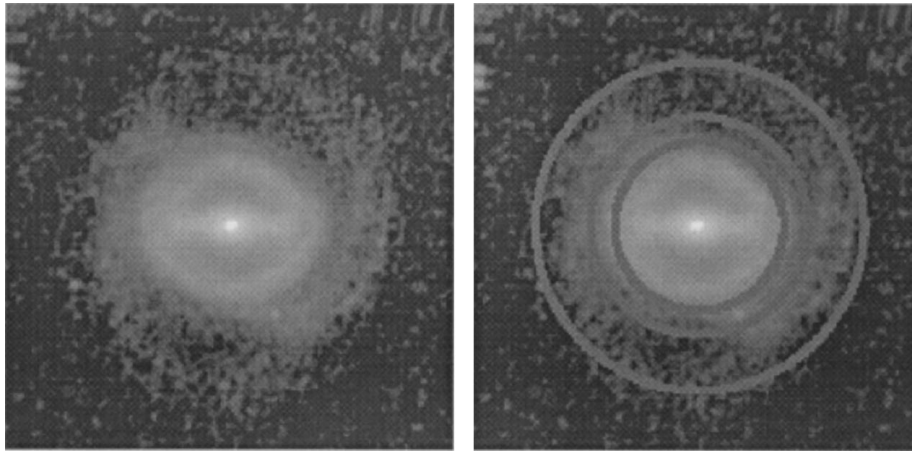


FIG. 13.—*Left*: Deprojected *B*-band image of IC 4290. *Right*: same image with resonance circles UHR (*innermost*), CR, and OLR (*outermost*) superposed.

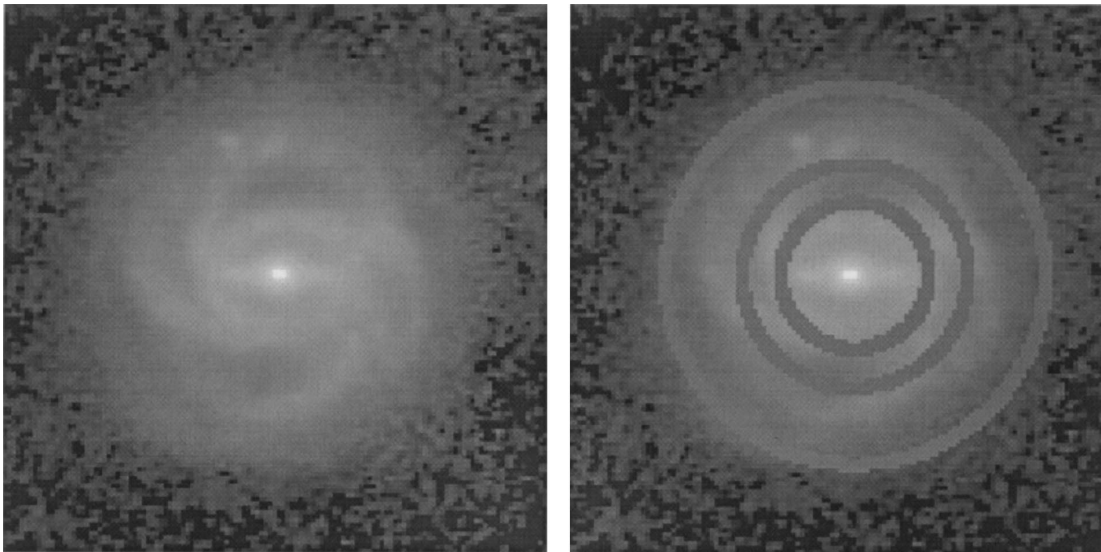


FIG. 14.—*Left*: Deprojected *B*-band image of ESO 566-24. *Right*: same image, with resonance circles UHR (*innermost*), CR, and OLR (*outermost*) superposed.

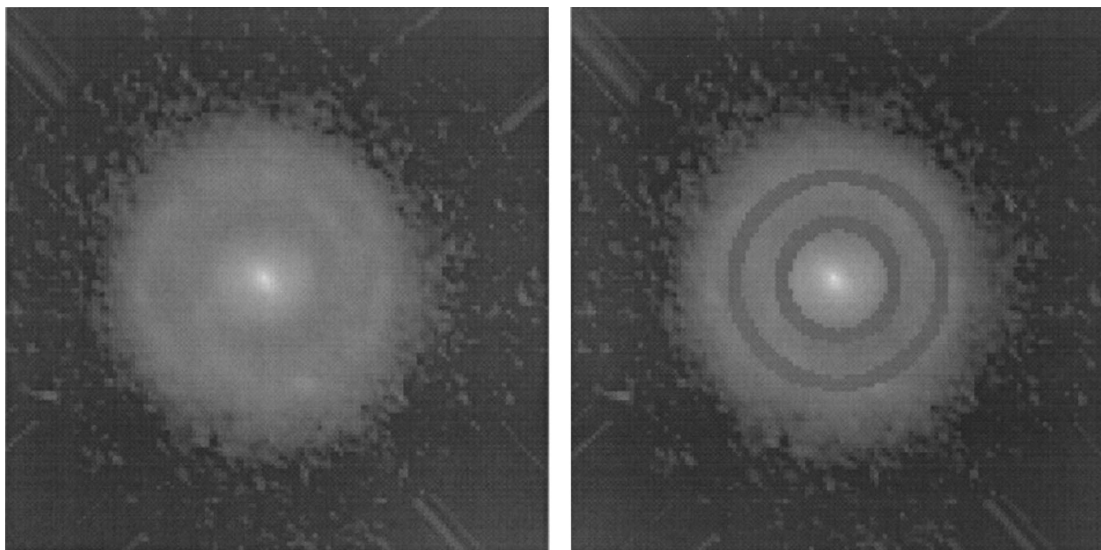


FIG. 15.—*Left*: Deprojected *B*-band image of ESO 509-98. *Right*: same image, with resonance circles CR (*innermost*) and OLR superposed

in blue light. The appearance suggests that the R_1R_2' morphology of this galaxy is defined by two spiral arms that begin at opposite points along the bar minor-axis line. The results of ellipse fits to visual mappings of the two features are listed in Table 6. Although the features have roughly perpendicular deprojected alignments (for the adopted orientation parameters $i = 52^\circ$, $\phi_n = 35^\circ$), their deprojected axis ratios are rounder than the averages for the same features from CSRG statistics. Use of the photometric major-axis position angle and the kinematic inclination as alternative orientation parameters changes these results slightly, as shown in Table 6.

8. GRAVITATIONAL POTENTIALS, DARK MATTER, AND PATTERN SPEEDS

In this final section, we use the near-IR images of our sample galaxies to derive information on the gravitational potentials of the systems. The principal assumption we make is that the H -band mass-to-light ratio is constant over most of the disk, such that the light traces the mass. In general, this will be a good assumption over most of the regions we are interested in, since near-IR colors tend to be fairly uniform with position in these early-type galaxies. Departures might be expected in the central regions and at large radii, and in particular in regions of strong recent star formation (Rhoades 1998). By comparing derived rotation curves with observed ones, we can evaluate the significance of dark matter over the regions of interest and deduce other properties of the systems.

The transformation of the disk H -band light distributions in our galaxies into gravitational potentials was performed using the methods outlined by Quillen, Frogel, & González (1996). The method uses a fast Fourier transformation on a rectangular coordinate grid and allows for the finite thickness of the disk. In each case, we have estimated, as in Quillen et al., the vertical scale height h of the disk as $(1/12)h_D$, where h_D is the radial exponential scale length in the near-IR. The resulting two-dimensional potential is expanded in Fourier series to derive the axisymmetric rotation curve and the relative contributions of higher order terms to the potential. In all four of our sample galaxies, the light distribution predicts a falling rotation curve at large radii that is either inconsistent with the observed rotation curve (IC 4290, ESO 566-24) or is likely to be inconsistent once a more extensive rotation curve is actually measured (NGC 1326, ESO 509-98). To improve the rotation curve fits, we have iterated for the parameters of a “fixed-sigma” halo model from Kent (1986) to keep the rotation curve flat or consistent with the observed rotation curve. From the final derived rotation-curve fit, we have computed the standard Lindblad precession frequencies $\Omega \pm \kappa/2$ and $\Omega - \kappa/4$, where Ω is the circular angular velocity and κ is the epicyclic frequency, to judge pattern speeds and resonance locations. Pattern speeds are only determined indirectly, since we will use assumptions about at least one of the observed rings in a given system to fix the pattern speed.

The H -band images were deprojected for the potential analysis using the IRAF routine IMLINTRAN in flux-conserving mode with the line of nodes position angles and inclinations adopted from the previous sections. Using the standard-star zero point of the H -band photometry and an absolute magnitude of +3.37 for the Sun at H (Worthey 1994), the deprojected images were converted to solar H -band luminosities per parsec². These images were then

passed through the gravitational potential program with an assumed mass-to-light ratio of 1.0 and the predicted rotation curves were compared (where possible) with the observed ones. These comparisons then readily gave the correct mass-to-light ratios required.

8.1. Bulge Decompositions

Three of our sample galaxies have significant bulges that had to be treated separately from the disk. For these cases, we performed decompositions using a variety of approaches so that we could transform the bulge profile into a rotation curve separately from the disk component.

For NGC 1326, we used the procedure outlined by Kent & Glauddell (1989), who analyzed images of the SB0 galaxy NGC 936. Our H -band image of NGC 1326 was deprojected according to our adopted orientation parameters, and rotated such that the major axis is horizontal. In the regions just outside the nuclear ring, this image shows elongated isophotes oriented along the minor axis, which we interpret to be the artificially stretched isophotes of the bulge. Following Kent & Glauddell (1989), we chose two position angles symmetrically placed around the deprojected bar minor-axis line, such that the contribution of the bar is the same along each position angle. Then an iterative procedure was used to extract the bulge profile, assuming a disk (major- to minor-axis) flattening of $f_D = 1.36$ and a bulge flattening of $f_B = 1.11$. We found that the resulting profile is well-described, at least in the radius range $1'' \leq r \leq 23''$, by an $r^{1/n}$ law with $n = 2.22$. The resulting profile extrapolated beyond $r = 23''$ is shown by the solid curve in Figure 6. Interestingly, Andredakis, Peletier, & Balcells (1996) obtained $n = 2.3$ for a sample of Sa-Sb galaxies.

In the case of ESO 509-98, we were able to use the much simpler procedure of Kent (1986) to extract the bulge profile. The bar of this galaxy is relatively weak compared with the other sample galaxies. For the decomposition, we used a disk flattening of 1.56 and a bulge flattening of 1.0. The resulting profile could be approximated by an exponential of small scalelength, and is shown by the solid curve in Figure 6. Note that a bulge flattening of 1.1 was also found to be acceptable for this galaxy; use of this flattening would reduce the amount of disk light in the central few arcseconds, compared with a flattening of 1.0.

For ESO 566-24, derivation of the bulge profile was complicated, because the bar major axis deprojects to within a few degrees of the minor axis. In this circumstance, neither the method of Kent (1986) nor that of Kent & Glauddell (1989) could be used to extract the bulge profile. Instead, we used an iterative procedure whereby the bar light distribution was modeled as a Gaussian curve perpendicular to its axis (see, e.g., Ohta, Hamabe, & Wakamatsu 1990; Ohta 1996). Profiles were taken in the deprojected H -band image along perpendicular cuts at radii of $\pm 11''$, where it appears that the bar dominates, and a mean bar minor-axis profile was computed from the average of these two profiles. Since the bar is superposed within a more uniform surface brightness lens (see Kormendy 1979), the contribution of this component to the light was iterated along the perpendicular cuts as an intensity offset so that the net bar minor-axis profile was Gaussian. Finally, a profile taken along the deprojected bar major axis of 179° was used to estimate the bar major-axis surface brightness. For $r \geq 11''$, the measured surface brightnesses were used, while for $r < 11''$, we set $\mu_{\text{bar}} = \mu_{\text{bar}}(11'')$. A model image of the Gaussian bar was

then created and subtracted from the deprojected image, which was then reprojected to the sky plane. Ellipses were fitted to the bar-subtracted bulge region after correction for a constant-lens surface brightness. This showed that the bulge is exponential within $r = 10''$ and has a mean projected axis ratio of 0.88. Further analysis suggested that the bar is not flat in brightness, but has ansae and therefore is enhanced near its ends. The final bulge model is shown in Figure 6.

In IC 4290, the bulge is clearly a smaller contribution to the total light at H than for the other sample galaxies. We therefore analyzed its potential as if the whole system were a disk. Higher resolution near-IR observations could perhaps

better separate this feature from the disk and bar components.

8.2. Disk Potentials and Nonaxisymmetric Components

The disk gravitational potentials were derived using vertical scale heights of 220, 355, 350, and 205 parsecs for NGC 1326, IC 4290, ESO 509-98, and ESO 566-24, respectively. These values were estimated from radial scale lengths and are necessarily uncertain, especially for ESO 509-98. Fourier analyses of these potential images led to the relative amplitudes shown in Figure 16 for each galaxy. These are computed from azimuthal averages of the potentials in circular annuli. For azimuthal numbers $m = 2, 4,$ and $6,$ the

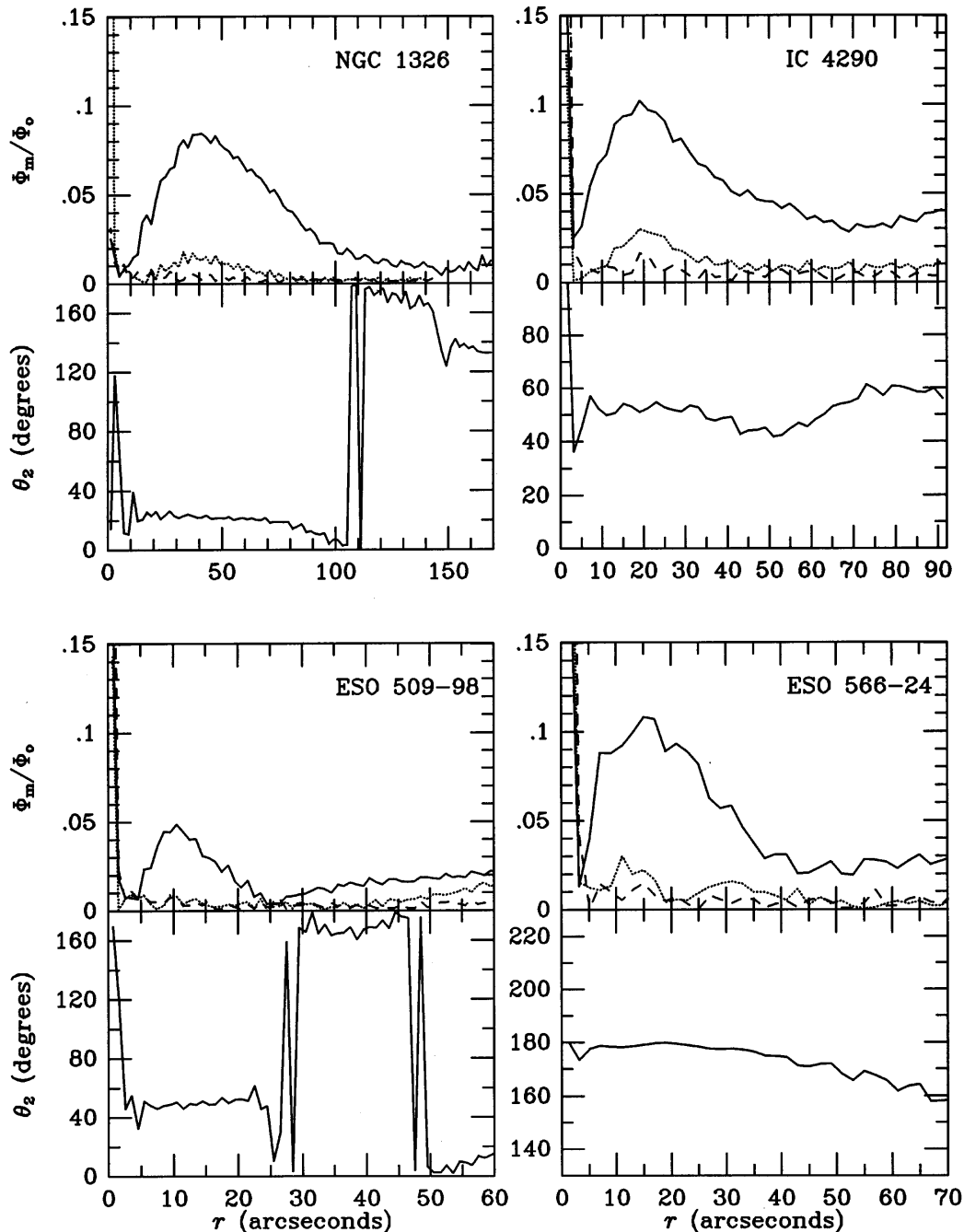


FIG. 16.—Relative amplitudes of the $m = 2$ (solid curves), 4 (dotted curves), and 6 (dashed curves) components of the gravitational potential in the four sample galaxies. The quantity θ_2 is the phase of the $m = 2$ component.

cosine and sine amplitudes Φ_{mc} and Φ_{ms} were computed as a function of radius and the relative amplitude computed as $(\Phi_{mc}^2 + \Phi_{ms}^2)^{1/2}/\Phi_0$, where Φ_0 is the average axisymmetric background. For each galaxy, the relative $m = 2$ amplitude (*solid curves*) increases to a maximum and then decreases at larger radii. The maxima achieved range from close to 0.1 for IC 4290 and ESO 566-24 to only 0.05 for ESO 509-98. Thus, the bars of these galaxies have maximum $m = 2$ amplitudes of up to only 10% of their respective disk axisymmetric backgrounds. Three of the galaxies also show significant $m = 4$ amplitude (*dotted curves*), especially IC

4290, whose bar displays a boxy character in the inner regions.

8.3. Predicted Rotation Curves and Lindblad Precession Frequencies

The gravitational potentials deduced from the H -band images were used to compute the rotation curve for each sample galaxy. The left panels of Figure 17 show “maximum disk/bulge” solutions where the observed rotation curve has been matched without any contribution from a halo component. For those galaxies where a bulge decom-

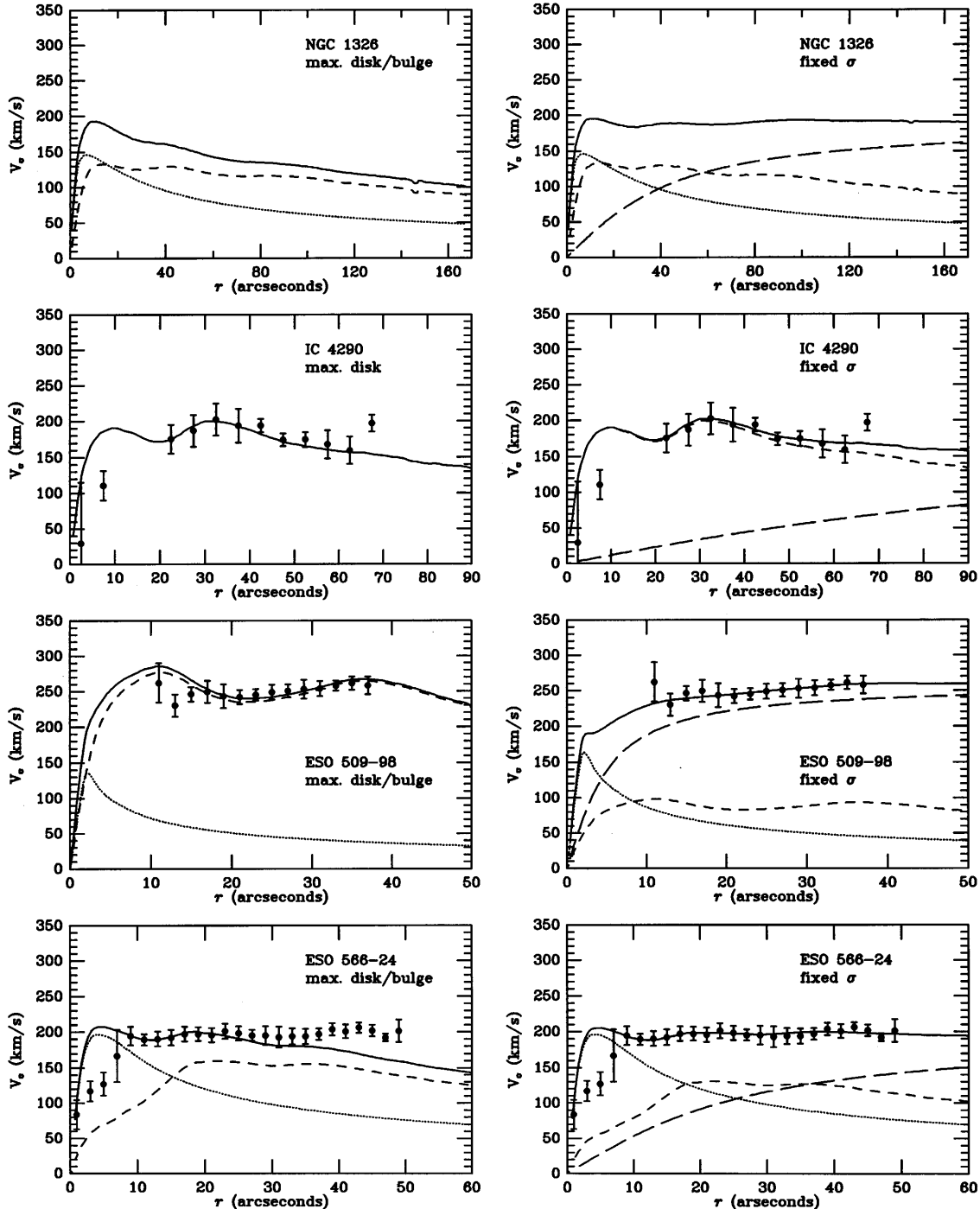


FIG. 17.—Rotation curve models of the four sample galaxies. Dotted curves refer to the bulge, dashed curves refer to the disk, while solid curves refer to the total model. In the right panels, long dashed curves refer to a “fixed- σ halo” model. Error bars on the observed points are 1σ standard deviations.

TABLE 7
RESULTS OF ROTATION CURVE ANALYSES

Parameter	NGC 1326	IC 4290	ESO 509-98	ESO 566-24
Maximum disk/bulge solutions:				
M/L_H (bulge)	0.5 ± 0.1	...	0.6 ± 0.1	0.9 ± 0.15
M/L_H (disk)	0.5 ± 0.1	1.4 ± 0.6	2.4 ± 0.4	0.9 ± 0.15
Fixed- σ solutions:				
M/L_H (bulge)	0.5 ± 0.1	...	0.9 ± 0.15	0.9 ± 0.15
M/L_H (disk)	0.5 ± 0.1	1.4 ± 0.6	0.3 ± 0.05	0.6 ± 0.1
a (arcseconds)	34 ± 6	85 ± 14	4.0 ± 1.5	20 ± 2
σ (km s^{-1})	134 ± 8	121 ± 14	183 ± 9	139 ± 7

position was performed, the rotation curve of the disk was computed from the radial derivative of Φ_0 , the axisymmetric part of the disk potential. The rotation curve of the bulge was computed using a program written by A. Kalnajs and S. M. G. Hughes that treats the bulge as a spheroid of specified flattening (c/a). In each case, the bulge was taken to be nearly spherical. The finite thickness of the disk was already accounted for in the computation of the disk potential. The separate predicted rotation curves were combined in quadrature to give the final rotation curve. For NGC 1326, the mass-to-light ratios are simply scalings to force a maximum rotation velocity of 190 km s^{-1} based on the galaxy's 21 cm line width from Bureau et al. (1996) reduced to an inclination of 43° . This is consistent within uncertainties with the rotation velocities measured along position angle 77° by Storchi-Bergmann et al. (1996), reduced to our adopted inclination and line of nodes position angle.

The mass-to-light ratios required to fit the observed curves are summarized in Table 7. The listed errors include the uncertainties in the distance estimates and inclinations, but not in the assumed scale heights. The average disk mass-to-light ratio obtained is 1.3 ± 0.8 , roughly consistent with the predicted value of 1.19 for a 12 Gyr single-burst theoretical stellar population model (Worthey 1994).

Figure 17 shows that maximum disk/bulge solutions work fairly well for IC 4290 and ESO 509-98. For ESO 566-24, the predicted rotation curve falls off from the observed one at radii beyond $20''$, and also fails to work for radii smaller than $9''$. For NGC 1326, it appears maximum disk/bulge solutions predict a falling rotation curve outside the nuclear ring. The rotation curve fits work better when a halo model is included. For this purpose, we used the fixed- σ model of Kent (1986). The advantage of this model is that the rotation curve asymptotes to a constant value at large radii, so that flat rotation curves are well-represented by such a model. The right panels of Figure 17 show the rotation curve fits with a fixed- σ halo model added in (see Table 7 for model parameters a and σ). For NGC 1326 and

ESO 566-24, we can obtain a very flat rotation curve with comparable contributions from the disk, bulge, and halo in the intermediate regions. Only a very extended halo is needed in the case of IC 4290, but in the case of ESO 509-98 the halo is the dominant required component.

We have used the fixed- σ model solutions to compute the circular angular velocity Ω , the epicyclic frequency κ , and the Lindblad precession frequencies, $\Omega \pm \kappa/2$ and $\Omega - \kappa/4$, for each of our sample galaxies (see Fig. 18). These curves are needed to locate the resonances in the disk in each galaxy. Figure 18 also shows the deprojected radii of the ring features in each galaxy, from Table 6. To fix the pattern speed, Ω_p , we have assumed that the outer rings or pseudo-rings in each galaxy are connected with the OLR. The resulting pattern speeds and locations of other resonances are listed in Table 8. The listed uncertainties on the various parameters of this table include our judgment of the uncertainty in r_{OLR} (bottom row) and, for Ω_p in absolute units, the uncertainty in the distance.

For NGC 1326, we have taken the location of the OLR to be at the outer apparent edge of the R_1 outer ring. This is reasonable, since the outer edge roughly coincides with a zone of bluer colors just outside this ring, reminiscent of what was seen in NGC 3081 by BP98. As for NGC 3081, this choice places corotation (CR) in the gap region between the inner and outer R_1 rings, the inner 4:1 resonance (UHR) near the radius of the inner ring, and the nuclear ring between two inner Lindblad resonances (ILRs; see Fig. 11, right panel, and Fig. 18, upper left panel). For IC 4290, the pattern speed was fixed by setting the radius of the R_1 outer pseudoring to the radius of the OLR. This choice places corotation well beyond the ends of the bright bar, but the inner ring is placed very close to the UHR (see Fig. 13, right panel, and Fig. 18, upper right panel). Note that in spite of the lack of any nuclear star formation or offset dust lanes in the bar, the model still predicts the existence of ILRs. For ESO 509-98, the position of the OLR was fixed by the average of the major-axis radius of the R_1 component and

TABLE 8
RESONANCE LOCATIONS

Parameter	NGC 1326	IC 4290	ESO 509-98	ESO 566-24
Ω_p ($\text{km s}^{-1} \text{ arcsec}^{-1}$)	3.2 ± 0.5	3.9 ± 0.7	16 ± 1.5	6.6 ± 1.1
Ω_p ($\text{km s}^{-1} \text{ kpc}^{-1}$)	43 ± 10	13 ± 5	32 ± 4	30 ± 6
r_{ILR} (arcsec)	2.2 ± 0.2	2.5 ± 0.3	2.1 ± 0.1	1.4 ± 0.2
r_{OILR} (arcsec)	19 ± 2	17 ± 1.5	3.4 ± 0.2	9.9 ± 1.1
r_{UHR} (arcsec)	36 ± 6	36 ± 10	8.6 ± 1.0	20 ± 4
r_{CR} (arcsec)	58 ± 8	46 ± 6	15 ± 1.5	30 ± 5
$r_{\text{CR}}/r_{\text{bar}}$	1.4 ± 0.2	1.7 ± 0.2	1.3 ± 0.15	1.8 ± 0.3
r_{OLR} (arcsec) (assumed)	102 ± 15	70 ± 10	28 ± 3	50 ± 8

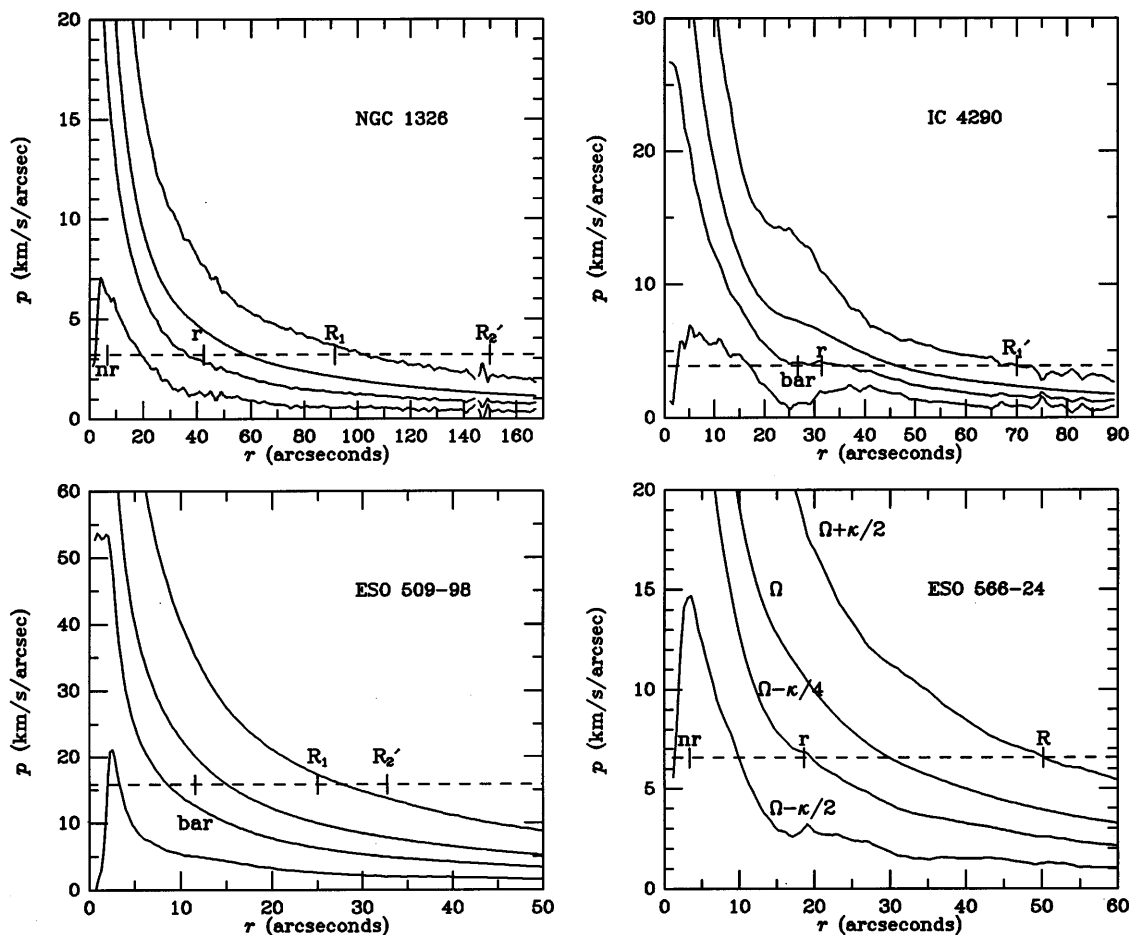


FIG. 18.—Precession frequency curves for the four sample galaxies. From left to right, the curves are $\Omega - \kappa/2$, $\Omega - \kappa/4$, Ω , and $\Omega + \kappa/2$, where Ω is the circular angular velocity and κ is the epicyclic frequency (see lower right panel). The horizontal dashed lines are the pattern speeds deduced by connecting outer ring or pseudoring features to the OLR. The deprojected major axis radii of various ring features are indicated, where “nr” represents a nuclear ring, “r” represents an inner ring, and “R₁,” “R₂,” “R₁’,” and “R” refer to various outer ring/pseudoring features.

the minor-axis radius of the R₂ component. This choice places CR just outside the ends of the bar (see Fig. 15, right panel, and Fig. 18, lower left panel). ESO 509-98 was presented by Byrd et al. (1994) as a probable high-pattern speed example, where ILRs and the UHR are avoided. Lacking adequate constraints, we cannot say that ILRs are not avoided, but the model suggests that the UHR is not avoided. However, the UHR is predicted to lie *inside* the bar, where an inner ring is less likely to form.

For ESO 566-24, the location of OLR is less clear. We find that if we locate OLR with the radius of the faint ring beyond the four-armed spiral pattern, then the pattern speed predicts UHR to be very close to the radius of the inner ring. ILRs are predicted to exist, and the small nuclear ring would lie between them. CR, however, is well beyond the ends of the bar and, in fact, lies in the midst of the four-armed pattern (see Fig. 14, right panel, and Fig. 18, lower right panel). The boundary of the four-armed zone would lie close to the outer UHR, where $\Omega_p = \Omega + \kappa/4$. This provides a possible interpretation of this pattern, though it is unclear why the outer UHR would be so prominent in this galaxy while it is not in general seen in other galaxies. The significance of the outer UHR is discussed briefly by Schwarz (1984b), and an alternative interpretation of how it might connect to rings is provided by Byrd et al. (1998).

The ratio of the predicted radius of corotation to the radius of the bar is an important quantity that has been computed for other galaxies (see a review by Elmegreen 1996). On average, $r_{\text{CR}}/r_{\text{bar}} = 1.2 \pm 0.2$. For our sample, the ratio is found to be 1.55 ± 0.2 . In these cases, CR is predicted to be well beyond the ends of the bar, an unexpected result. BP98 obtained a more extreme ratio of 2.2 for NGC 3081.

9. SUMMARY

In this paper, we have presented surface photometry at optical and near-infrared wavelengths of four excellent early-type ringed galaxies. Kinematic information is also provided for three of these galaxies. From these observations, we have deduced the following:

1. The four galaxies are very diverse in their properties. Luminosity profiles are complex and multihumped. The profiles of ESO 509-98 are most distinct in showing a large zone of uniform surface brightness followed by a steep decline in surface brightness at larger radii.
2. Three of the sample galaxies have inner rings. When these galaxies are deprojected according to their measured orientation parameters, the inner rings align parallel to the bars with intrinsic axis ratios ranging from 0.7 to 0.8, consistent with the results of CSRG statistics.

3. The strong outer ring of NGC 1326 deprojects into a nearly perpendicular alignment with the bar, based on photometric orientation parameters determined from the shapes of deep red continuum isophotes. This alignment is very similar to what was found for NGC 3081 by BP98. The intrinsic axis ratio, 0.83, of the feature is nearly the same as the average for SB galaxies from CSRG statistics. However, the bar in NGC 1326 is weak in blue light, owing to a complex dust pattern covering much of the bar.

4. When an exponential background of light is subtracted from the optical images, two of our sample galaxies, NGC 1326 and ESO 566-24, reveal evidence for an additional ringlike feature at large radii.

5. Rotation curves for three of the galaxies are normal in shape with good symmetry. When the *H*-band light distribution is converted into a rotation curve, two of the galaxies show evidence for the presence of a dark matter halo.

6. A resonance analysis of the rotation curves (in the epicyclic approximation) indicates that consistency between

ring locations can be obtained for a single pattern speed in each case. Under the assumption that an outer ring or pseudoring feature is connected with the OLR, the inner rings in three of the sample galaxies are located near the inner 4:1 ultraharmonic resonance, consistent with the test particle models of Schwarz (1984a, 1984b).

We thank A. Quillen and A. Kalnajs for allowing us to use their programs to compute rotation curves for our sample galaxies, and also an anonymous referee for many helpful comments and suggestions. R. B., D. A. C., and G. B. P. gratefully acknowledge the support of NSF grants AST 90-14137 and AST 96-17154 to the University of Alabama during the course of this work. M. L. and A. J. A. gratefully acknowledge support from NSF Research Experiences for Undergraduates (REU) grant 94-24226, also to the University of Alabama, during the summers of 1995 and 1996, respectively.

REFERENCES

- Aaronson, M., Huchra, J., Mould, J., Schechter, P., & Tully, R. B. 1982, *ApJ*, 258, 64
- Aaronson, M., Mould, J. R., & Huchra, J. P. 1980, *ApJ*, 237, 655
- Andredakis, Y., Peletier, R., & Balcells, M. 1996, in *IAU Colloq. 157, Barred Galaxies* ed. R. Buta, D. Crocker, & B. Elmegreen (ASP Conf. Ser. 91) (San Francisco: ASP), 86
- Athanassoula, E., Morin, S., Wozniak, H., Puy, D., Pierce, M. J., Lombard, J., & Bosma, A. 1990, *MNRAS*, 245, 130
- Bessell, M. S. 1989, *PASP*, 91, 589
- Bureau, M., Mould, J. R., & Staveley-Smith, L. 1996, *ApJ*, 463, 60
- Buta, R. 1985, *Proc. Astron. Soc. Australia*, 6, 56
- . 1995, *ApJS*, 96, 39 (CSRG)
- Buta, R., & Crocker, D. A. 1991, *AJ*, 102, 1715 (BC91)
- . 1992, *AJ*, 103, 1804 (BC92)
- . 1993, *AJ*, 105, 1344
- Buta, R., & Purcell, G. B. 1998, *AJ*, 115, 484 (BP98)
- Byrd, G. G., Ousley, D., & Dalla Piazza, C. 1998, *MNRAS*, in press
- Byrd, G., Rautiainen, P., Salo, H., Buta, R., & Crocker, D. A. 1994, *AJ*, 108, 476
- Cardelli, J. A., Clayton, G. C., & Mathis, J. S. 1989, *ApJ*, 345, 245
- Corwin, H. G., de Vaucouleurs, A., & de Vaucouleurs, G. 1985, *Southern Galaxy Catalogue*, Univ. of Texas Monographs in Astron. No. 4
- Crocker, D. A., Baugus, P. D., & Buta, R. 1996, *ApJS*, 105, 353 (CBB96)
- de Vaucouleurs, A., & Longo, G. 1988, *Catalog of Visual and Infrared Photometry of Galaxies from 0.5 μ m to 10 μ m (1961–1985)*, Univ. of Texas Monographs in Astron. No. 5
- de Vaucouleurs, G. 1974, in *IAU Symp. No. 58, The Formation and Dynamics of Galaxies*, ed. J. R. Shakeshaft (Dordrecht: Reidel), 335
- de Vaucouleurs, G., de Vaucouleurs, A., Corwin, H. G., Jr., Buta, R. J., Paturel, G., & Fouqué, P. 1991, *Third Reference Catalogue of Bright Galaxies* (New York: Springer)
- D'Onofrio, M., Capaccioli, M., Zaggia, S. R., & Caon, N. 1997, *MNRAS*, 289, 847
- Elias, J. H., Frogel, J. A., Matthews, K., & Neugebauer, G. 1982, *AJ*, 87, 1029
- Elmegreen, B. G. 1996, in *IAU Colloq. 157, Barred Galaxies* ed. R. Buta, D. Crocker, & B. Elmegreen (ASP Conf. Ser. 91) (San Francisco: ASP), 197
- Ferrarese, L., et al. 1996, *ApJ*, 464, 568
- Fouqué, P., Bottinelli, L., Gouguenheim, L., & Paturel, G. 1990, *ApJ*, 349, 1
- Friedli, D., Wozniak, H., Rieke, M., Martinet, L., & Bratschi, P. 1996, *A&AS*, 118, 461
- García-Barreto, J., Dettmar, R.-J., Combes, F., Gerin, M., & Koribalski, B. 1991, *Rev. Mexicana Astron. Astrofis.*, 22, 197
- Gonzalez, A. H., & Faber, S. M. 1997, *ApJ*, 485, 80
- Graham, J. A. 1982, *PASP*, 94, 244
- Hubble, E. 1926, *ApJ*, 64, 321
- Kennicutt, R. C., Tamblyn, P., & Congdon, C. W. 1994, *ApJ*, 435, 22
- Kent, S. M. 1986, *AJ*, 91, 1301
- Kent, S. M., & Glaudell, G. 1989, *AJ*, 98, 1588
- Kormendy, J. 1979, *ApJ*, 227, 714
- Landolt, A. U. 1992, *AJ*, 104, 340
- Lauberts, A. 1982, *The ESO/Uppsala Survey of the ESO (B) Atlas (Garching: ESO)*
- Maia, M. A. G., da Costa, L. N., & Latham, D. W. 1989, *ApJS*, 69, 809
- Maia, M. A. G., da Costa, L. N., Willmer, C., Pellegrini, P. S., & Rit e, C. 1987, *AJ*, 93, 546
- Mebold, U., Goss, W. M., van Woerden, H., Hawarden, T. G., & Siegman, B. 1979, *A&A*, 74, 100
- Ohta, K. 1996, in *IAU Colloq. 157, Barred Galaxies* ed. R. Buta, D. Crocker, & B. Elmegreen (ASP Conf. Ser. 91) (San Francisco: ASP), 37
- Ohta, K., Hamabe, M., & Wakamatsu, K. 1990, *ApJ*, 357, 71
- Phillips, A. C., Illingworth, G. D., MacKenty, J. W., & Franx, M. 1996, *AJ*, 111, 1566
- Pierce, M. J., McClure, R. D., & Racine, R. 1992, *ApJ*, 393, 523
- Pierce, M. J., & Tully, R. B. 1992, *ApJ*, 387, 47
- Quillen, A. C., Frogel, J. A., & González, R. A. 1996, *ApJ*, 437, 162
- Rautiainen, P., Salo, H., Byrd, G., Buta, R., & Crocker, D. A. 1996, in *IAU Colloq. 157, Barred Galaxies*, ed. R. Buta, D. Crocker, & B. Elmegreen (ASP Conf. Ser. 91) (San Francisco: ASP), 483
- Rhoades, J. E. 1998, *AJ*, 115, 472
- Sandage, A., & Bedke, J. 1994, *The Carnegie Atlas of Galaxies (Washington: Carnegie Inst. Washington)*
- Sandage, A., & Tammann, G. 1995, *ApJ*, 446, 1
- Schommer, R. A., Bothun, G. D., Williams, T. B., & Mould, J. R. 1993, *AJ*, 105, 97
- Schwarz, M. P. 1981, *ApJ*, 247, 77
- . 1984a, *MNRAS*, 209, 93
- . 1984b, *Proc. Astron. Soc. Australia*, 5, 464
- Shaw, M., Axon, D., Probst, R., & Gatley, I. 1995, *MNRAS*, 274, 369
- Storchi-Bergmann, T., Rodríguez, A., Schmitt, H. R., Wilson, A. S., & Baldwin, J. A. 1996, *ApJ*, 472, 83
- van Moorsel, G. A., & Wells, D. C. 1985, *AJ*, 90, 1038
- Warner, P. J., Wright, M. C. H., & Baldwin, J. E. 1973, *MNRAS*, 163, 163
- Worthey, G. 1994, *ApJS*, 95, 107
- Wozniak, H., Friedli, D., Martinet, L., Martin, P., & Bratschi, P. 1995, *A&AS*, 111, 115

ERRATUM: “AN OPTICAL, NEAR-INFRARED, AND KINEMATIC STUDY OF FOUR EARLY-TYPE
RESONANCE RING GALAXIES” [ASTRON. J. 116, 1142 (1998)]

R. BUTA

Department of Physics and Astronomy, University of Alabama

ADINA J. ALPERT

Department of Physics and Astronomy, University of Pennsylvania

MELINDA LEWIS COBB

Department of Physics, Muskingum College

AND

D. A. CROCKER AND GUY B. PURCELL

Department of Physics and Astronomy, University of Alabama

Received 2000 March 14; accepted 2000 April 7

An error was discovered in the zero point used for the *H*-band photometry of the galaxy ESO 566-24 in this paper. An exposure time of 6 s per co-add frame was used instead of the actual 8 s. To correct for the mistake, a constant of +0.31 mag should be added to the total *H*-band magnitude and surface brightnesses for the galaxy in Table 1 and in Figure 6 (*bottom right*). The mass-to-light ratios for the galaxy in Table 7 should also be increased by 30%. The other galaxies in the paper are not affected by the mistake, and the basic conclusions of the paper are not impacted by it.

R. B. would like to thank D. L. Block for bringing his attention to this mistake.